

ALMA MATER STUDIORUM · UNIVERSITÀ DI BOLOGNA

---

SCUOLA DI SCIENZE

Corso di Laurea in Environmental Assessment and Management

The satellite  
detection of  
marine plastic debris

Relatore:  
Chiar.mo Prof.  
NADIA PINARDI

Presentata da:  
FRANCA PELUSI

Sessione  
Anno Accademico 2021/2022

*A mio fratello Nicola  
a lui dedico i miei più grandi successi*

# Abstract

This work aims to evaluate whether it is possible to detect plastic on the sea surface with the use of satellite images. High resolution multispectral optical data from our study area were obtained from the European Space Agency under the Copernicus program. The study area is the Po River Delta, one of the largest river deltas in the Mediterranean, located in the Veneto region of Emilia Romagna which flows into the northern Adriatic Sea after completing its course which starts from Monviso and crosses the entire Plain. Padana. Floating aggregations were detected using an optimized algorithm (floating debris index). An algorithm that exploits the difference between NIR and the base reflectance of NIR. After processing the scanned images, the searched information is extracted. Macroplastics are often mixed with natural materials such as algae or foam. Two indices are used to try to classify the different materials: a normalized differential vegetation index and the floating debris index. However, this process is not always linear. Clouds and rough seas can compromise data and macroplastics move fast. To validate the functioning of the algorithm used, a bibliographic search was carried out, from which information was obtained in which there was certainty of the presence of macroplastics in situ. And thanks to these studies, we were able to understand if the algorithm works and to what degree of accuracy. In particular, satellite images were collected from the MARIDA dataset (Kikaki et al. 2020) and from the following studies: Biermann et al. 2020 and Topouzelis et al 2019. Among the most important findings is that we have shown that aggregate plastic spots can be detected by satellites.

# Contents

<b>Contents</b>	<b>3</b>
<b>List of Figures</b>	<b>4</b>
<b>List of Tables</b>	<b>10</b>
<b>1 Introduction</b>	<b>11</b>
1.0.1 The role of plastic pollution for the healthy ocean . . . . .	12
1.0.2 Overview of detection capabilities and methodologies . . . . .	17
1.0.3 Objectives of the thesis . . . . .	23
<b>2 Analysis methods</b>	<b>24</b>
2.1 Description of analysis software . . . . .	24
2.1.1 Sentinel Application Platform (SNAP) . . . . .	31
2.1.2 Floating debris index . . . . .	32
2.1.3 Normalised Difference Vegetation Index . . . . .	33
2.2 . . . . .	34
<b>3 Reproduction/validation of the marine plastic debris detection methods</b>	<b>39</b>
3.0.1 The Biermann case . . . . .	42
3.0.2 The Topouzelis case . . . . .	46
3.0.3 The Marida case . . . . .	47
<b>4 New study cases for the Po river coastal area</b>	<b>57</b>
4.0.1 Satellite images . . . . .	57
<b>5 Conclusions</b>	<b>62</b>
<b>6 Bibliography</b>	<b>64</b>
<b>7 Acknowledgements</b>	<b>66</b>

# List of Figures

1.1	Production of plastics in Europe and worldwide from 1950 to 2015 (MMT) (Statistics 2017) . . . . .	12
1.2	Cumulative plastic waste generation and disposal (in million metric tons). Solid lines show historical data from 1950 to 2015; dashed lines show projections of historical trends to 2050. . . . .	13
1.3	The image portrays an example of the interaction between marine vertebrates and plastic waste abandoned in the environment (www.oggiscienza.it) . . . . .	15
1.4	The image portrays an example of interaction between marine vertebrates and plastic waste abandoned in the environment (www.greenme.it) . . .	15
1.5	Reported number of entanglements / ingestion by taxonomic group. Charts show total number of individuals (a.), Total number of species (b.), And total papers involving marine debris entanglement / ingestion (SCBD, 2012). 16	
1.6	Reported incidents of entrapment / ingestion of marine debris by decade (SCBD, 2012) . . . . .	17
1.7	Caption . . . . .	18
1.8	Electromagnetic spectrum . . . . .	19
1.9	comparison between the spectral signatures of different types of surfaces. Source: <a href="http://www.alspergis.altervista.org/lezione/05.html">http://www.alspergis.altervista.org/lezione/05.html</a> . . . . .	19
1.10	Remote sensors interception of reflected incident radiation. Source: <a href="https://www.docenti.unina.it/be/allegati/materiale-didattico/562052">https://www.docenti.unina.it/be/allegati/materiale-didattico/562052</a> . . . . .	20
1.11	digital image with particular of the Pixel and Digital number that the make up. Source: google . . . . .	21
2.1	Copernicus open access hub . . . . .	25
2.2	Advanced search . . . . .	26
2.3	Sentinel model 2, source: wikipedia . . . . .	27
2.4	. . . . .	28

2.5	Spectral bands made available in MSI products (VNIR: Visible and Near Infra-Red, SWIR: Short Wave Infra-Red) . . . . .	28
2.6	The Universal Transverse Mercator (UTM) system divides the earth's surface into 60 distinct time zones. Each spindle has a vertical width of longitude 6° and is divided into 20 bands each having a horizontal width of latitude 8°, thus generating 1200 UTM zones. The zones are marked with a number ranging from 1 to 60 (indicating the time zone) and a letter ranging from C to X (indicating the band). . . . .	29
2.7	SNAP 8.0 interface . . . . .	31
2.8	The selected bands for detecting floating debris are highlighted in bold. (Biermann et al. 2020) . . . . .	32
2.9	FDI index (Biermann et al. 2020) . . . . .	33
2.10	NDVI index . . . . .	34
2.11	Spectral signatures derived from the mean spectra of deployed plastic targets (black line with error bars), seaweed representing floating vascular plants (green), seawater from all test sites (dashed blue line), rafted timber and wood representing non-photosynthetic plant materials (red), pumice representing non-plant debris (light grey), and spume representing sea foam, bubbles and froth (gold line). The x-axis shows the span of Sentinel-2 MSI bands from visible blue light at 490 nm, to short-wave infrared light at 1610 nm. The left-hand y-axis shows remote sensing reflectance (unitless) from Sentinel-2 for seawater, seaweed, sea foam and the plastic targets. Remote sensing reflectance (unitless) of timber and pumice was substantially higher. These were shifted lower to illustrate relative spectral shapes of all materials, and the corresponding reflectances are shown on the right hand y-axis in grey. (Biermann et al. 2020) . . . . .	36
2.12	Classifying known floating materials in the marine environment. Using NDVI alone (a), we see that clear seawater (blue), wood (dark grey), spume (gold) and pumice (light grey) occupy distinct NDVI ranges that do not overlap with the combined (grouped) plastics. (Biermann et al. 2020) . . . . .	38

- 3.1 **Image representing FDI-NDVI-RGB. Satellite image of the Accra, Ghana on 31 October 2018. Tile:30NZM. Time of acquisition 10:11:39, time of processing 13:56:33. Image was captured by Sentinel-2 B multispectral instrument** (a) FDI (Floating Debris Index). In red all the pixels that assume the values included in the FDI range, (b)NDVI (Normalized Difference Vegetation Index). In yellow all the pixels that assume the values included in the NDVI range, (c) True color R (590-670) nm, G (500-590) nm, B (455-515) . . . . . 42
- 3.2 **Image representing FDI-NDVI-RGB. Satellite image of the Accra, Ghana on 31 October 2018. Tile:30NYM. Time of acquisition 10:11:39, time of processing 13:56:33. Image was captured by Sentinel-2 B multispectral instrument** (a) FDI (Floating Debris Index). In red all the pixels that assume the values included in the FDI range, (b)NDVI (Normalized Difference Vegetation Index). In yellow all the pixels that assume the values included in the NDVI range, (c) True color R (590-670) nm, G (500-590) nm, B (455-515) . . . . . 43
- 3.3 **Image representing FDI-NDVI-RGB. Satellite image of the Gulf Islands, Canada on 18 July 2018. Tile:30UDV. Time of acquisition 19:19:49, time of processing 22:37:20. Image was captured by Sentinel-2 B multispectral instrument** (a) FDI (Floating Debris Index). In red all the pixels that assume the values included in the FDI range, (b)NDVI (Normalized Difference Vegetation Index). In yellow all the pixels that assume the values included in the NDVI range, (c) True color R (590-670) nm, G (500-590) nm, B (455-515) . . . . . 44
- 3.4 **Image representing FDI-NDVI-RGB. Satellite image of the Scotland, UK on 20 April 2018. Tile:30VWH. Time of acquisition 11:21:21, time of processing 11:44:17. Image was captured by Sentinel-2 B multispectral instrument** (a) FDI (Floating Debris Index). In red all the pixels that assume the values included in the FDI range, (b)NDVI (Normalized Difference Vegetation Index). In yellow all the pixels that assume the values included in the NDVI range, (c) True color R (590-670) nm, G (500-590) nm, B (455-515) . . . . . 45

- 3.5 **Image representing FDI-NDVI-RGB. Satellite image of Mytilene, Greece on 7 June 2018. Tile:35SMD. Time of acquisition 08:56:01, time of processing 11:05:13. Image was captured by Sentinel-2 B multispectral instrument** (a) FDI (Floating Debris Index). In red all the pixels that assume the values included in the FDI range, (b)NDVI (Normalized Difference Vegetation Index). In yellow all the pixels that assume the values included in the NDVI range, (c) True color R (590-670) nm, G (500-590) nm, B (455-515) . . . . . 47
- 3.6 **Image representing FDI-NDVI-RGB. Satellite image of Guatemala on 18 september 2020. Tile:16PCC. Time of acquisition 16:08:39, time of processing 19:45:32. Image was captured by Sentinel-2 B multispectral instrument** (a) FDI (Floating Debris Index). In red all the pixels that assume the values included in the FDI range, (b)NDVI (Normalized Difference Vegetation Index). In yellow all the pixels that assume the values included in the NDVI range, (c) True color R (590-670) nm, G (500-590) nm, B (455-515) . . . . . 48
- 3.7 **Image representing FDI-NDVI-RGB. Satellite image of C.America, Guatemala on 16 June 2018. Tile:16PCC. Time of acquisition 16:09:01, time of processing 21:19:42. Image was captured by Sentinel-2 B multispectral instrument** (a) FDI (Floating Debris Index). In red all the pixels that assume the values included in the FDI range, (b)NDVI (Normalized Difference Vegetation Index). In yellow all the pixels that assume the values included in the NDVI range, (c) True color R (590-670) nm, G (500-590) nm, B (455-515) . . . . . 49
- 3.8 **Image representing FDI-NDVI-RGB. Satellite image of C.America/Honduras on 18 September 2020. Tile:16PDC. Time of acquisition 16:08:39, time of processing 19:45:32. Image was captured by Sentinel-2 B multispectral instrument** (a) FDI (Floating Debris Index). In red all the pixels that assume the values included in the FDI range, (b)NDVI (Normalized Difference Vegetation Index). In yellow all the pixels that assume the values included in the NDVI range, (c) True color R (590-670) nm, G (500-590) nm, B (455-515) . . . . . 50

- 3.9 **Image representing FDI-NDVI-RGB. Satellite image of C.America/Honduras on 23 September 2020. Tile:16QED. Time of acquisition 16:10:11, time of processing 20:11:18. Image was captured by Sentinel-2 B multispectral instrument** (a) FDI (Floating Debris Index). In red all the pixels that assume the values included in the FDI range, (b)NDVI (Normalized Difference Vegetation Index). In yellow all the pixels that assume the values included in the NDVI range, (c) True color R (590-670) nm, G (500-590) nm, B (455-515) . . . . . 51
- 3.10 **Image representing FDI-NDVI-RGB. Satellite image of C.America/Honduras on 29 November 2015. Tile:16PEC. Time of acquisition 16:16:22, time of processing 16:26:44. Image was captured by Sentinel-2 B multispectral instrument** (a) FDI (Floating Debris Index). In red all the pixels that assume the values included in the FDI range, (b)NDVI (Normalized Difference Vegetation Index). In yellow all the pixels that assume the values included in the NDVI range, (c) True color R (590-670) nm, G (500-590) nm, B (455-515) . . . . . 52
- 3.11 **Image representing FDI-NDVI-RGB. Satellite image of Asia,Indonesia on 4 March 2018. Tile:50LLR. Time of acquisition 02:15:59, time of processing 05:50:41. Image was captured by Sentinel-2 B multispectral instrument** (a) FDI (Floating Debris Index). In red all the pixels that assume the values included in the FDI range, (b)NDVI (Normalized Difference Vegetation Index). In yellow all the pixels that assume the values included in the NDVI range, (c) True color R (590-670) nm, G (500-590) nm, B (455-515) . . . . . 53
- 3.12 Percentage pixel coverage of the floating plastic targets . . . . . 54
- 3.13 Pixel detection legend and methodology . . . . . 54
- 4.1 **Combined display of FDI-NDVI-RGB in large scale of the study area. The purple circle indicates the area where a possible accumulation of floating material has been detected. Satellite image of the Padana area of 26 August 2021.** Time of acquisition 10:05:49, time of processing 12:15:47. Image was captured by Sentinel-2B multispectral instrument. (a) FDI (Floating Debris Index). In red all the pixels that assume the values included in the FDI range. (b)NDVI (Normalized Difference Vegetation Index). In yellow all the pixels that assume the values included in the NDVI range. (c) True color R (590-670) nm, G (500-590) nm, B (455-515) . . . . . 58

4.2	<b>Combined display of FDI-NDVI-RGB of the area indicated inside the circle in the previous image. Satellite image of the Padana area of 26 August 2021.</b> Time of acquisition 10:05:49, time of processing 12:15:47. Image was captured by Sentinel-2B multispectral instrument. (a) FDI (Floating Debris Index). In red all the pixels that assume the values included in the FDI range. (b)NDVI (Normalized Difference Vegetation Index). In yellow all the pixels that assume the values included in the NDVI range. (c) True color R (590-670) nm, G (500-590) nm, B (455-515) . . . . .	59
4.3	NDVI plotting containing only the pixels that fall within the specific range of values indicated in table 3.1. . . . .	60
4.4	Plotting of FDI containing only the pixels that fall within the specific range of values indicated in table 3.1. . . . .	60
4.5	Plotting of the interpolation of the two matrices. . . . .	61

# List of Tables

3.1	Biermann range of pixel values . . . . .	40
3.2	<b>The plastic debris events detected by the three studies based on satellite and in situ data.</b> Images used for validation with related information available. . . . .	41
3.3	<b>NDVI and FDI values of the three targets.</b> In green the values of both algorithms that fall within the range and are consequently classified as plastic. In yellow the values that only for one of the two algorithms fall within the range. The last column indicates the % coverage of the target within the pixel. . . . .	55
3.4	Only verified pixel of the Marida dataset . . . . .	55
4.1	<b>Aquisition Dates.</b> Dates in which the satellite images used in this work were acquired. . . . .	57

# Chapter 1

## Introduction

Plastic has now become an omnipresent material in our life and in our economy. Plastic is used for a wide range of purposes due to its affordability, versatility, strength, and light weight. However, we are unable to properly and efficiently recycle all the plastic we continue to use. Worldwide, it is estimated that between 4 and 12 million tons of plastic enter the oceans each year, mainly from coastal inputs (Boucher and Friot, 2017; Jambeck et al., 2015; Neufeld et al., 2016). Plastic pollution is an emerging environmental risk affecting human health, livelihoods and ecosystems (van Emmerik & Schwarz, 2020). Rivers carry most of the plastic in the oceans and are also (temporary) reservoirs of plastic cargoes (Meijer, van Emmerik, van der Ent, Schmidt, & Lebreton, 2021). Plastic is nowadays one of the main sources of environmental pollution, particularly in the seas. Taking into account the plastic balance it results that every year 4.8 - 12.7 million tons of macroplastics waste observed at sea enter the sea (Lebreton, et al., 2017; Meijer, van Emmerik, van der Ent, Schmidt, & Lebreton, 2021). Currently, however, direct monitoring of rivers is practically absent. The only exception is monitoring through physical sampling using trawl nets and nets, visual counting from bridges or river banks or techniques based on images obtained through the use of cameras or unmanned aerial vehicles (UAVs) (Castro-Jiménez, GonzálezFernández, Fornier, Schmidt, & Sempéré, 2019; Roebroek, van Emmerik, González, & Laufkötter, 2022). These monitoring techniques are often labor intensive and therefore difficult to scale at the river basin level, continental or global. As a result, their geographic coverage is limited and data is not collected consistently over time and space. The use of these techniques has identified a plastic flow of many orders lower than that hypothesized by the empirical models mentioned above. There is therefore an important inconsistency in the mass balance of plastic. In any case, the quantity of material that arrives annually in the oceans is very high and, for this reason, the possibility of monitoring and quantifying these flows of plastic material exiting the watercourses through the use of satellite

data, whose measurement capacity in this area remains currently minimally explored. Hence, direct monitoring of macroplastics in rivers by satellite would help quantify and explore this issue. The reasons that prompted me to tackle this issue derive from the responsibility I feel to help and preserve the marine environment, a precious treasure to be safeguarded. Contributing to the preservation of nature is a great satisfaction. This paper is organized as follows: chapter 1 presents an introduction to the history of the production of plastic materials over the years; post-use management, where they end up and what are its effects on human health and the environment; recalls the fundamental concepts of remote sensing, considering it useful to provide a general framework for this discipline. Chapter 2 describes the different softwares used for viewing and processing satellite data. Chapter 3 describes the elaboration put in place to verify the effectiveness of the methodology used. Chapter 4 describes the application of the model in the waters leaving the river Po. The thesis ends with a discussion on the opportunities and limits of such applications in the future.

### 1.0.1 The role of plastic pollution for the healthy ocean

In just a few decades, plastics have radically changed economy and society, becoming an essential element in the modern life. Combining excellent functional properties, such as low weight, high strength, wide application range, easy processability on an industrial scale, with low cost, these materials are omnipresent and have outgrown most manmade materials (European Commission, 2019; Geyer et al., 2017).

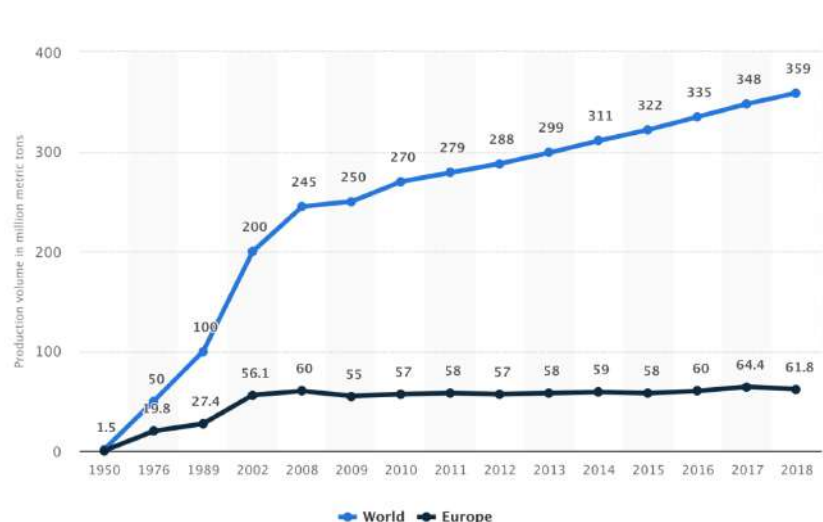


Figure 1.1: Production of plastics in Europe and worldwide from 1950 to 2015 (MMT) (Statistics 2017)

Commercial production of plastics started around 1950's, when the innovations in

material field dictated by military needs to find substitutes for natural not available products, invade the civil world. Since this moment, plastics production has enjoyed exceptional growth and, between 1950 and 2015, an estimated 8.3 billion tonnes of plastics were produced, of which 6.3 billion tonnes are considered as waste (Geyer et al., 2017). In 2018 global plastics production reached 359 million tonnes (figure 2.1) with 61.8 million tonnes generated in Europe alone (PlasticsEurope— The Facts 2019). At the present rate of growth, worldwide plastics production is estimated to double within the next 20 years (Lebreton and Andrady, 2019). The image shows the projection up to 2050 of the current global trends in waste management (fig. 2.2), 9000 Mt of plastic waste will have been recycled, 12,000 Mt incinerated and 12,000 Mt discarded in landfills or in the environment. (source: Geyer et al., 2017)

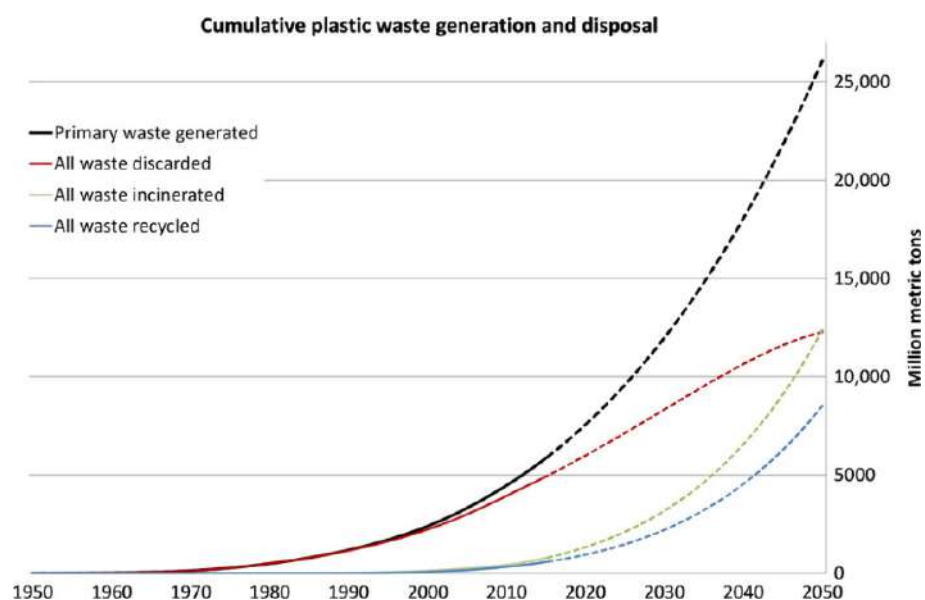


Figure 1.2: Cumulative plastic waste generation and disposal (in million metric tons). Solid lines show historical data from 1950 to 2015; dashed lines show projections of historical trends to 2050.

The marine environment represents a natural resource of vital importance for the planet. Marine and ocean ecosystems are home to vast biodiversity, and yet human well-being is linked strictly to the sea and its resources, man has altered its balance over the last few centuries. Fishing, pollution, deep sea exploration for hydrocarbons, ocean acidification and warming of ocean temperatures accompanied by sea level rise as a consequence of glacier melting (IPCC 2004) are important examples referring to the pressure that humans exert on marine environments, which determine negative ecological and socio-economic repercussions.

During the recent decades the presence of anthropogenic waste, which represents

one of the main sources of pollution of the oceans, has been identified as one of the most serious environmental problems of global interest. The “Marine Litter” is defined as “any solid material discarded, manufactured or transformed, disposed of or abandoned in a marine or coastal environment”. It consists of objects, often disposable, used by people and deliberately discarded in rivers, at sea, on beaches, transported by rivers, wastewater, rainwater or winds, or those accidentally lost (UNEP, 2009).

The presence of litter in the sea was first mentioned in the scientific literature in 1960, and the numerous researches that followed stated a steady increase in the amount of debris in ocean ecosystems. Several studies have shown that the main material of waste is plastic, associated with a continuous increase in annual global production of 299 million tons (PlasticsEurope, 2015).

It is well established that marine litter and in particular plastics affects marine organisms and habitats. Species and ecosystems can be exposed to marine environmental plastic litter via a variety of exposure pathways including ingestion, entanglement, smothering, and the rafting and introduction of invasive species. (John S.Woods 2019 et.al.) Each years, millions of animals that live in the oceans are debilitated mutilated and killed by marine litter (Butterworth et. Al., 2012). Marine litter has been demonstrated to have deleterious impact on individuals, with direct lethal or sublethal effects. It seems inevitable that entanglement and ingestion by/of marine debris will alter the biological and ecological performance of individuals, compromising and the individual’s ability to capture food, digest food, sense hunger, escape from predators, and to reproduce, as well as decreasing body condition and compromising locomotion, including migration (CBD 2012). With the transport of floating plastic there is also a potential problem that is often overlooked: the transport and introduction of invasive species (NOAA, 2015). Biofilms of algae, bacteria and cyanobacteria can colonize floating debris and thrive in the marine environment. Bio-foulers including barnacles, mussels and macroalgae can attach to surfaces of large debris and travel.



Figure 1.3: The image portrays an example of the interaction between marine vertebrates and plastic waste abandoned in the environment ([www.oggiscienza.it](http://www.oggiscienza.it))



Figure 1.4: The image portrays an example of interaction between marine vertebrates and plastic waste abandoned in the environment ([www.greenme.it](http://www.greenme.it))

In 2012, the Secretariat of the Convention on Biological Diversity (SCBD) found the majority of reported marine debris pollution (MDP) entanglement and ingestion cases were caused by plastic debris (figure 2.6)

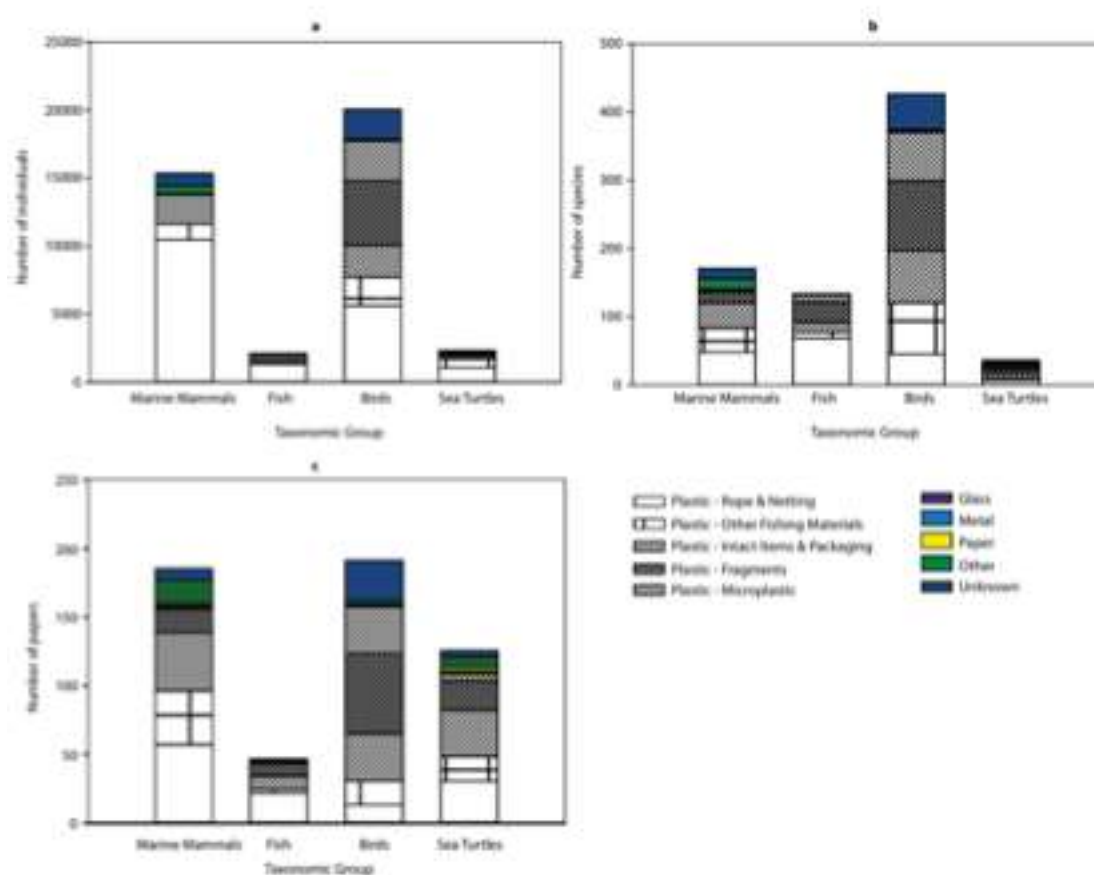


Figure 1.5: Reported number of entanglements / ingestion by taxonomic group. Charts show total number of individuals (a.), Total number of species (b.), And total papers involving marine debris entanglement / ingestion (SCBD, 2012).

Just over a decade ago, the number of marine species known to be impacted by anthropogenic litter was estimated at around 260 species (Derraik, 2002). Now, the number of marine species with reports of fatal entanglement in and ingestion of marine debris has risen to nearly 700, and continues to increase (Gall and Thompson, 2015)

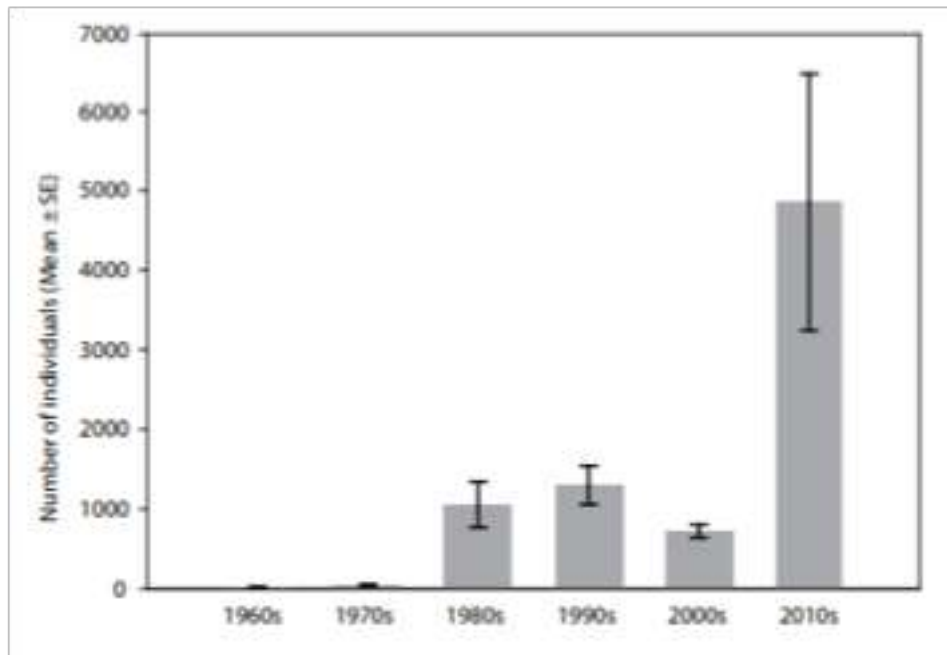


Figure 1.6: Reported incidents of entrapment / ingestion of marine debris by decade (SCBD, 2012)

## 1.0.2 Overview of detection capabilities and methodologies

### Remote sensing

Remote sensing can be considered as the set of techniques, tools and interpretative means that allow you to extend the perceptive capabilities of the human eye by providing the observer with both qualitative and quantitative information on objects placed at a distance.

Remote sensing measures electromagnetic energy coming from the surfaces in question, that is, it quantifies the alterations that the object imposes on the radiation, or its characteristics of intensity, frequency, and polarization. Furthermore, without disturbing the observed object, it has the advantage of obtaining information:

1. *Synoptics* that is, a high spatial coverage and instant observation of large areas are obtained;
2. *Dinamics* as it is possible to acquire data at different times in the same area of interest;
3. *Homogeneous* as there is consistency of the data.

## Electromagnetic Wave

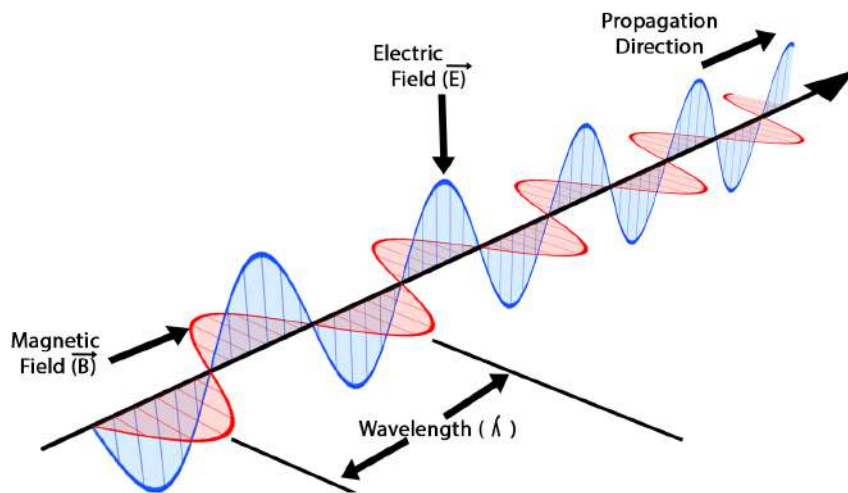


Figure 1.7: Caption

The reactions that occur inside the sun give rise, in accordance with Plank's black body law, to a complex spectrum of electromagnetic energy, which reaches the earth attenuated by the phenomena of reflection, diffusion and absorption due to the atmosphere. The electromagnetic spectrum is defined as the continuous set of waves electromagnetic ordered according to their frequency, length or wave number. By convention, the electromagnetic spectrum has been divided, according to the wavelength, into spectral regions or bands, starting from the shorter wavelengths (gamma rays) up to radio waves. The visible region (between  $0.4 \mu\text{m}$  and  $0.7 \mu\text{m}$ ) includes the wavelengths perceived by the human eye and is divided into colors. The infrared region (between  $0.7 \mu\text{m}$  and  $1 \text{mm}$ ) can be divided, as the wavelength increases, into Near IR (near infrared), Mid IR (medium infrared) and Far IR (far infrared). In Figure 3.3 the regions of the spectrum are shown electromagnetic.

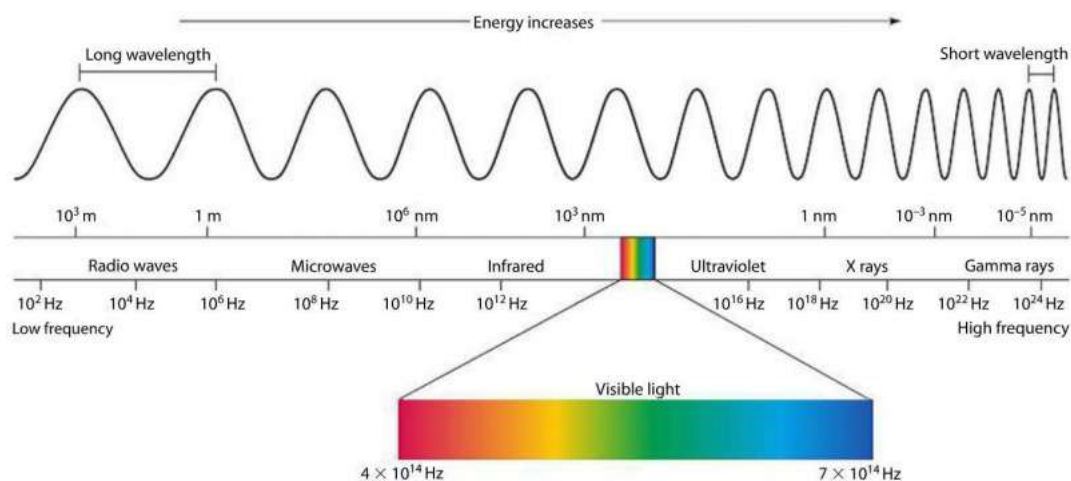


Figure 1.8: Electromagnetic spectrum

The electromagnetic radiation reflected, absorbed and transmitted by any object varies with the variation of the wavelength. In remote sensing, the reflectance term indicates the percentage of incident radiant energy that is reflected by a body and depends on the type of surface, the nature and the material of which it is composed. For each surface, therefore, a graph of the spectral signature or spectral response, characteristic of the surface itself, can be constructed, which highlights its reflection capabilities as a function of the wavelength of the incident radiation (Figure 3.4).

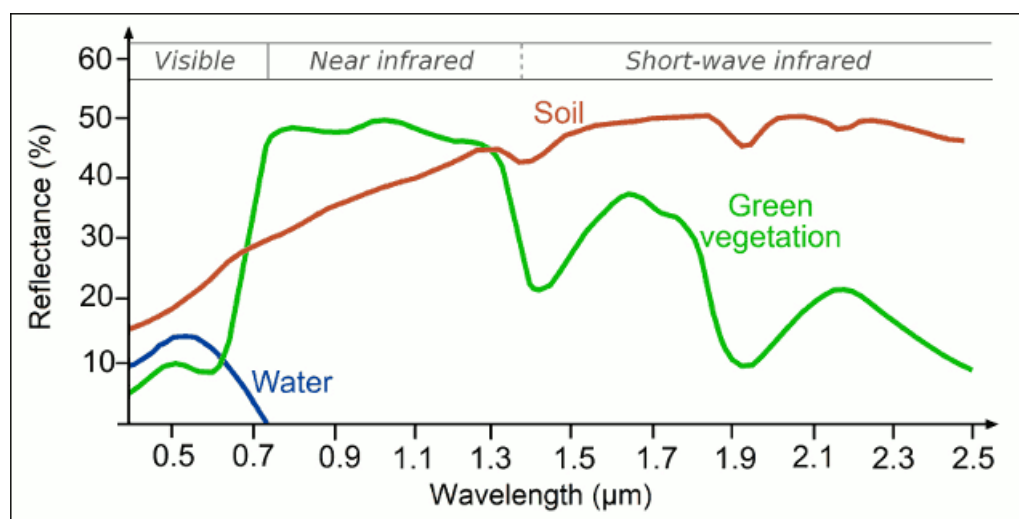


Figure 1.9: comparison between the spectral signatures of different types of surfaces.  
Source: <http://www.alspergis.altervista.org/lezione/05.html>

Each type of surface is therefore characterized by its own average spectral signature with a particular reflectance trend, with maximum and minimum values located in specific wavelength ranges.

Through remote sensing it is possible to study the electromagnetic radiation reflected or emitted by an object and the tools used to detect and then analyze this radiation are the remote sensors (figure 3.5)

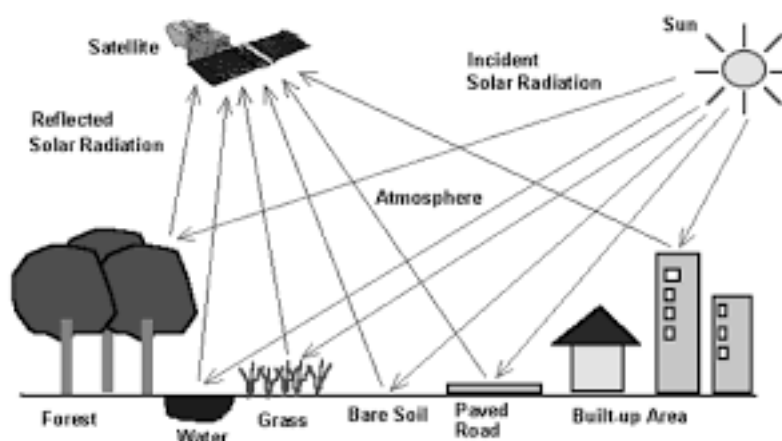


Figure 1.10: Remote sensors interception of reflected incident radiation. Source: <https://www.docenti.unina.it/webdocenti-be/allegati/materiale-didattico/562052>

These can be placed on land platforms, balloons, air and space vehicles. The distance between the shooting sensor and the investigated surfaces can vary from a few meters from the ground level (Proximal sensing) to a few kilometers (Remote sensing) in observations by air, up to distances of hundreds or thousands of kilometers, in the case of satellite platforms. The sensors are divided into passive and active. Passive sensors are those that detect the energy naturally reflected (solar) or that emitted (thermal) by the surface of the objects while the sensors that record the spectral responses to a source of artificial radiation coming from the instrument itself are active.

The quality of a sensor is defined by the radiometric resolution, by the geometric resolution, from the spectral and temporal resolution. The radiometric resolution indicates the sensitivity of the detector, of a certain sensor, in perceiving and encoding in signal the differences in radiant flux, reflected or emitted, from the surfaces analyzed. It is measured in bits and represents the number of levels into which the original signal can be broken down.

The geometric resolution indicates the dimensions of the elementary area on the ground of which the electromagnetic energy is detected and measured in meters. The spectral resolution is determined by the bandwidth (wavelength range) that the instrument is able to discriminate. Basically there are two types of sensors: multispectral and hyperspectral; the former record the image in a limited number of distinct spectral bands (usually less than ten), the seconds acquire the signal in numerous narrow and

close wavelength intervals, allowing to obtain a detailed spectral response of the various objects examined.

To allow accurate identification of objects, the spectral resolution of the sensor must be as comparable as possible with the spectral signature of the object itself. The time resolution indicates the time necessary for a sensor to make two consecutive shots of the same area.

The radiation recorded by the sensors is processed into a digital image. The digital image is a two-dimensional function defined by a regular grid pattern (geometric resolution) and the values it can assume belong to a positive integer range (radiometric resolution). It is therefore constituted by a set of discrete elements organized in rows and columns (matrix): to each of these elements, called pixels (picture element), is associated with a positive integer, digital number (DN), which represents the average radiance measured over a small area (resolution unit cell).

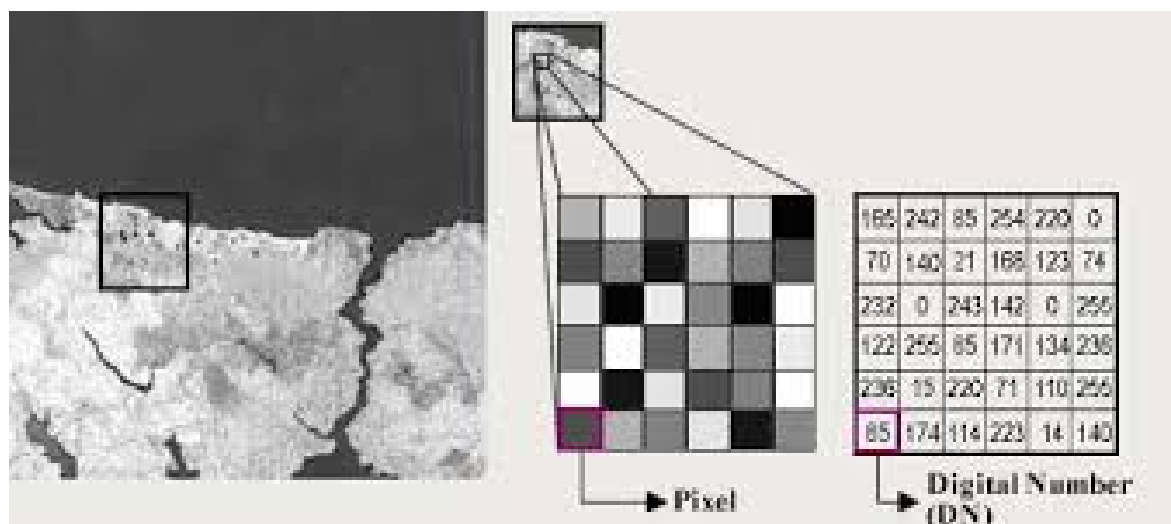


Figure 1.11: digital image with particular of the Pixel and Digital number that the make up. Source: google

Before being used, the images obtained from the remote sensors must be subjected to a pre-processing (image processing) in order to correct the "noise" present in the same due to the distortions and errors introduced during the acquisition phase.

The fundamental corrections, aimed at obtaining a representation, as faithful as possible, are the geometric and radiometric ones. The geometric correction eliminates the effects related to the characteristics of the system (sensor, platform, ground), eliminating errors in the localization of the pixels, placing them in their correct position within the image. Radiometric correction includes system corrections and atmospheric corrections. The former allow to cancel the shooting distortions and to calibrate the

sensors. The atmospheric corrections are used to eliminate the error determined by the layer of atmosphere interposed between the sensor and the investigated area, in fact, not all solar radiation reflected from the earth's surface reaches the sensors, since the atmosphere functions as a selective filter at different lengths wave.

The classification of remotely sensed images, through the spectral information, represented by digital numbers in one or more bands, is the most used procedure to assign all the pixels of an image to certain classes (water, forest, dry ground, wet ground, etc.). The image thus classified is composed of a mosaic of pixels, each of which belongs to a class, and essentially constitutes a thematic map of the starting image. When it comes to classes, it is appropriate to distinguish between information classes and spectral classes. The first are the types of interest that we try to identify in the image. The latter, on the other hand, are groups of uniform or very similar pixels, in the different spectral bands. The goal is to associate the spectral classes with the information classes of interest.

The classification methods can be divided into guided (Supervised classification) and non (Unsupervised classification).

The uncontrolled technique does not require prior knowledge of the elements to be discriminated, but is based only on the pixel values of the image, aggregating the data in clusters (continuous set of pixels assigned to the same class).

The guided procedure exploits the a priori definition of the thematic classes (end-member) of interest: the identification on the image of some sample areas, representative of the categories of interest (ROI: Region Of Interest), allows to determine the relative statistical parameters to the thematic classes chosen according to the pixel values belonging to the sample areas. In this way, the typical spectra of each class are identified (training sites) with which the classification of the entire scene is performed, comparing the image pixels and the spectral responses of the classes of interest, according to the similarity criterion adopted (classification algorithm).

A very delicate phase in the production of thematic maps obtained from remote sensing data is represented by the quality control of the classification, as it must provide an index of map accuracy. From the literature it was possible to ascertain that among the verification procedures the use of the "confusion matrix" (Congalton, 1991; Stehman et al., 1998; Foody, 2002) or "contingency matrix", which compares the membership class observed with the assignment category in the classified image. Not all remote sensing works report an assessment on the quality of the classification (Lucas et al., 2008; Asner et al., 2008); when this estimate is present, it appears to be very variable, especially depending on the application being studied.

### 1.0.3 Objectives of the thesis

Although marine plastic is a global problem, the Mediterranean Sea has been identified as one of the most polluted areas (van Sebille et al., 2015). This is worrying because the Mediterranean Sea is a hotspot for marine biodiversity and is home to 4% to 18% of the world's marine species (Bianchi and Morri, 2000). Research into plastic detection can be very useful work to help answer key questions about sources, paths, and trends and aid subsequent remediation actions. Because, if not removed, macroplastics can damage marine life by entrapment or ingestion, but they inevitably fragment and degrade into microplastics. Satellites that collect optical data offer a unique perspective from which to observe the problem of plastic waste in the marine environment, but few studies have successfully demonstrated their use for this purpose. This study aims to use satellite data for the identification of plastics, evaluate the functioning of the algorithm used and identify the oceanographic, climatic and meteorological conditions that can lead to possible accumulations of debris in the Mediterranean. The study examines the area of the Po Delta, the largest freshwater contribution of the Adriatic Sea. Rivers are the main route for anthropogenic waste (Lebreton et al., 2017; Schmidt et al., 2017). In this context, the study of the Po delta offers the opportunity to identify and evaluate a possible source of debris probably linked to the presence of adjacent cities, industrial settlements, and not least to the size of the surrounding population.

The objectives of the paper are the reproduction / validation of the satellite detection method and subsequently we will try to develop the first maps of Sentinel 2 plastic debris in the Po Valley.

# Chapter 2

## Analysis methods

### 2.1 Description of analysis software

#### Data acquisition

The images were downloaded through the Copernicus Open Access Hub program funded by the European Commission. Thanks to this program we have access to high resolution satellite data from a series of sensors. This data is available and completely free. Copernicus is currently the most ambitious Earth observation program in the world and consists of different systems (satellites, ground stations, air and marine sensors) that acquire data on Earth, as reported on the ESA website.

This program provides accurate, timely and easily accessible information to improve environmental management, understand and mitigate the effects of climate change and ensure civil safety. The program is coordinated and managed by the European Commission, while the development of the infrastructures takes place under the control of ESA as regards the space components. The thematic areas in which the services related to the Copernicus program are inserted are six:

- territory
- sea
- atmosphere
- climate change
- emergency management
- safety

These services support an infinite number of applications that include environmental protection, urban area management, land use planning, agriculture, forest management, fishing, transport, sustainable development, civil protection and tourism.

In this thesis the use of Sentinel data is aimed at the study of marine waters, for which particular attention should be paid to the theme of Copernicus marine services (CMEMS), which provides periodic and systematic reference information on the physical and biogeochemical state, on the variability and on the dynamics of oceanic and marine ecosystems for all the oceans of the world and the seas of the European region.

The next paragraph will be entirely dedicated to the description of the Sentinel project and the satellites, with particular attention to the Sentinel 1 and Sentinel 2 satellites, whose images will be used and analyzed in this thesis.

The data were downloaded free of charge from the special ESA servers and are available at the web address <https://scihub.copernicus.eu/> which presents itself with the following interface.



Figure 2.1: Copernicus open access hub

In this portal it is possible to select the area of interest (yellow rectangle) and carry out an advanced search thanks to the window on the left of the screen (figure 4.3) from which it is possible to choose the mission, the acquisition period, cloud cover..

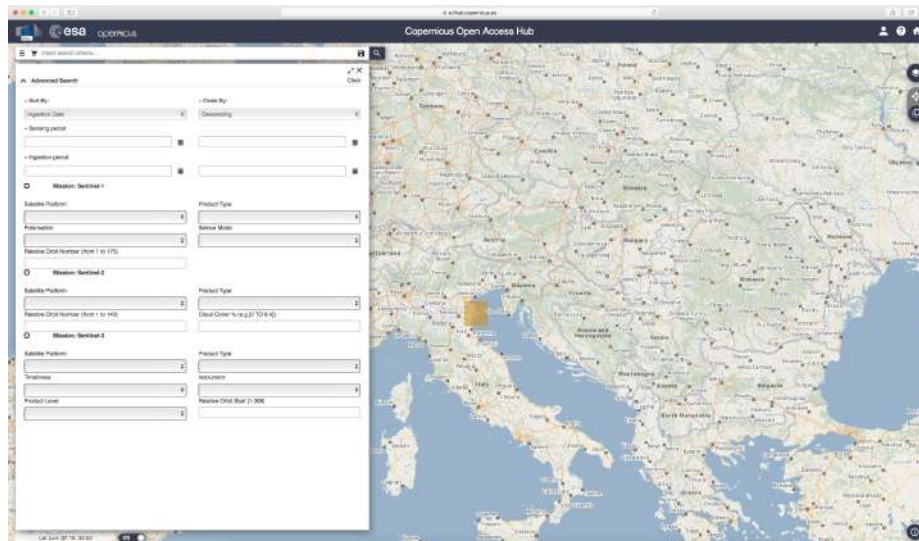


Figure 2.2: Advanced search

The Copernicus program has always used data from various space missions for its purposes. The primary purpose of the Sentinel satellites is to support the operational needs of the Global Monitoring for Environmental Security (GMES) program (Malenowsky et al., 2012).

## Sentinel-2

The data used in this thesis come from sentinel-2A and 2B satellites. The Sentinel-2 mission consists of two multispectral platforms, the first Sentinel-2A was launched into orbit on June 23, 2015, while the second launch took place on March 7, 2017. The Sentinel-2 mission provides multi-spectral images (13 bands) with high and medium spatial resolution depending on the specific band.

The satellites weigh approximately 1200 kg and are designed for a useful life of approximately 7 years, although the batteries and propellants have been charged for 12 years of operation, including the instrument's end-of-life orbital maneuvers.



Figure 2.3: Sentinel model 2, source: wikipedia

The MSI (Multispectral INstrument) sensors mounted on the platform work passively, the incident light rays are divided and filtered on separate focal planes, one for the visible bands (VIS), one for the near infrared band (NearInfraredNIR) and one for “short wave” infrared (Short Wave Infrared SWIR). A special mechanism, a sort of shutter, prevents the sensors from being hit by rays coming directly from the sun, the same mechanism also functions as a calibration tool by collecting the sun’s rays after reflection through a diffuser.

The two satellites operate on the same orbit inclined at  $98.62^\circ$  (with respect to the equator), sun-synchronous, at an average elevation of 786 km, out of phase by  $180^\circ$ . The choice of the sun-synchronous orbit was made because in this way the impact of shading on the ground is minimized.

The orbit is kept stable by a dedicated propulsion system and through the measurements of a dual-frequency GNSS receiver. They are designed so that the revisitation frequency is 5 days at the equator (2-3 days at medium latitudes) in the same grip conditions, this value decreases if we refer to different grip conditions, due to the lateral overlap of the acquisitions.

Sentinel-2 satellites are both equipped with a multispectral device (MSI) capable of receiving information on 13 spectral bands at different spatial resolutions, as shown in the following table (four bands at 10 metres, six bands at 20 metres and three bands at 60 metres spatial resolution.)

Table 1. Central wavelength value for Sentinel-2A and Sentinel-2B satellite multispectral instrument (MSI) bands.

MSI Bands	Description	Sentinel-2A Central Wavelength (nm)	Sentinel-2B Central Wavelength (nm)	Spatial Resolution (m)
Band 1	Coastal Aerosol	442.7	442.3	60
Band 2	Blue	492.4	492.1	10
Band 3	Green	559.8	559	10
Band 4	Red	664.6	665	10
Band 5	Red Edge 1	704.1	703.8	20
Band 6	Red Edge 2	740.5	739.1	20
Band 7	Red Edge 3	782.8	779.7	20
Band 8	Near Infrared (NIR)	832.8	833	10
Band 8A	Narrow NIR	864.7	864	20
Band 9	Water Vapour	945.1	943.2	60
Band 10	Short Wave Infrared (SWIR) Cirrus	1373.5	1376.9	60
Band 11	SWIR 1	1613.7	1610.4	20
Band 12	SWIR 2	2202.4	2185.7	20

Figure 2.4

The Multi-Spectral Instruments (MSI) aboard Sentinel-2A and 2B work passively, and optical data is acquired along the orbital path at high spatial resolution over land and adjoining coastal waters.

Sentinel-2 Multi-Spectral Instrument (MSI) products consist of a series of  $n$  granules each of which consists of 13 images (1 per spectral band) in JPEG-2000 format, divided between 3 preset spatial resolutions of 10m, 20m and 60m (see Figure 2.3).

- In products with ortho-photographic / cartographic correction (i.e. 1C e 2A) each granule, called tile in this specific case, covers an area of 100Km<sup>2</sup> in UTM / WGS84 projection. These types of products are associated with meta-data for georeferencing.
- In level 0, 1A and 1B products, each grain consists of an image which covers an area of 25Km<sup>2</sup>. Furthermore, level 0 and 1B products are not available to the public as they consist of raw images and therefore difficult to use.

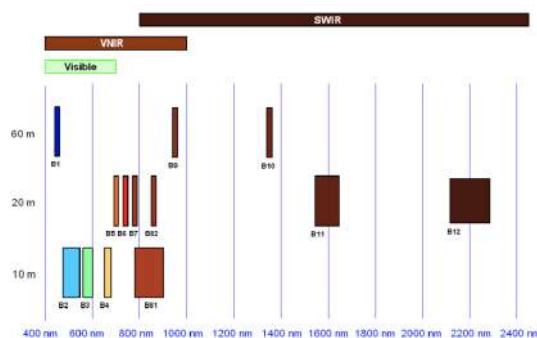


Figure 2.5: Spectral bands made available in MSI products (VNIR: Visible and Near Infra-Red, SWIR: Short Wave Infra-Red)

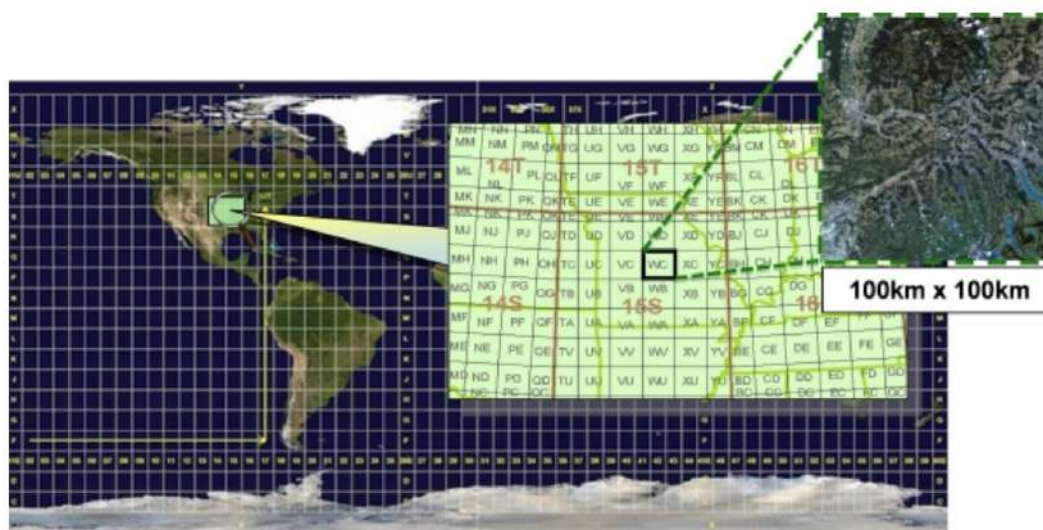


Figure 2.6: The Universal Transverse Mercator (UTM) system divides the earth's surface into 60 distinct time zones. Each spindle has a vertical width of longitude  $6^\circ$  and is divided into 20 bands each having a horizontal width of latitude  $8^\circ$ , thus generating 1200 UTM zones. The zones are marked with a number ranging from 1 to 60 (indicating the time zone) and a letter ranging from C to X (indicating the band).

- Level 0 products: These products consist of images compressed in ISP format. Inside they are composed of meta-data describing the product, data for the consistency of the compressed image and data necessary for the subsequent levels (for example the data for the processing of the geometric model, correlation data, thermal data, ephemeral(?) data and positional data).
- Level 1A products: These products are obtained by decompressing the images provided by level 0 products, on which the geometric model is then developed to map the position of all the pixels present in the image. The coordinates of the pixels in these packets are referred to their hypothetical center.
- Level 1B products: For level 1A products, to be qualified at level 1B, radiometric image correction must be applied in terms of correction of the reflection coefficient at Top of Atmosphere (TOA) and sensor geometry. Radiometric correction consists in: correction of dark signals, inhomogeneity of pixels, correction of defective pixels by interpolating them with neighboring pixels, restoration of high resolution bands. In addition, this type of product contains the geometric patterns perfected to produce level 1C images.
- Level 1C products: This level of products are generated from 1B images using

Digital Elevation (DEM) models to project the image into a cartographic / ortho-photographic reference system. The radiometric measurements for each pixel are provided in the form of the Top of Atmosphere reflection coefficient, together with the parameters to transform these values into radiance. These products are sampled with a constant Ground Sampling Distance (GSD) of 10m, 20m or 60m depending on the spectral bands to which they are related. In this case the coordinates of each pixel are referred to the edge in top left of the pixel. Level 1C products also contain land-related masks, water, clouds, and ECWF (total values of ozone and water vapor, level mean atmospheric pressure at sea level).

- Level 2A products: Level 2A products provide images with a correct reflection coefficient at Bottom of Atmosphere and with correction of clouds and water vapor through the use of masks made available by level 1C products from which they are derived.

Level 1C products were downloaded for this study.

### **Atmospheric correction**

Atmospheric correction represents one of the most critical issues in the pre-processing of satellite images.

The electromagnetic waves that reach the ground interact with the earth's atmosphere, and in particular with gases (carbon dioxide, oxygen, ozone, etc.), water vapor and the fine dust found in it. This interaction depends both on the length of the path that the wave takes before reaching the sensor, and on the atmospheric conditions at the time of observation. The processes of radiative interaction in the atmosphere of main interest for the purposes of remote sensing are scattering and absorption.

The scattering phenomenon occurs through the interaction of fine or gaseous particles in the atmosphere with electromagnetic radiation, which produces the diffusion of the electromagnetic waves themselves. The scattering effect, as regards the acquisition of remote sensing images, results in a lower contrast of the objects on the ground.

The atmospheric correction models take into account the radiative transfer processes briefly described and can be applied to remotely sensed data to reduce or remove their effects.

The inherent optical properties (IOPs) of floating materials can be leveraged for detection in Sentinel-2 imagery if NIR to SWIR wavelengths are conserved during the atmospheric correction process<sup>16</sup>.

Ocean and atmospheric components (scattering and absorption) were subtracted from surface reflectance values using ACOLITE (Atmospheric Correction for OLI lite

version 20181210.0).

Output for surface reflectance ( $\rho_{s}$ ) was computed using ACOLITE and visualised in the Sentinel Application Platform (SNAP) for further processing.

### 2.1.1 Sentinel Application Platform (SNAP)

SNAP version 8.0 software was used to analyze the images, which was created specifically for Sentinel image processing and analysis.

#### ESA-SNAP 8.0

SNAP is a software for the processing of satellite images produced and distributed free of charge from ESA, was created with the specific intent of treating the images coming from Sentinel platforms.

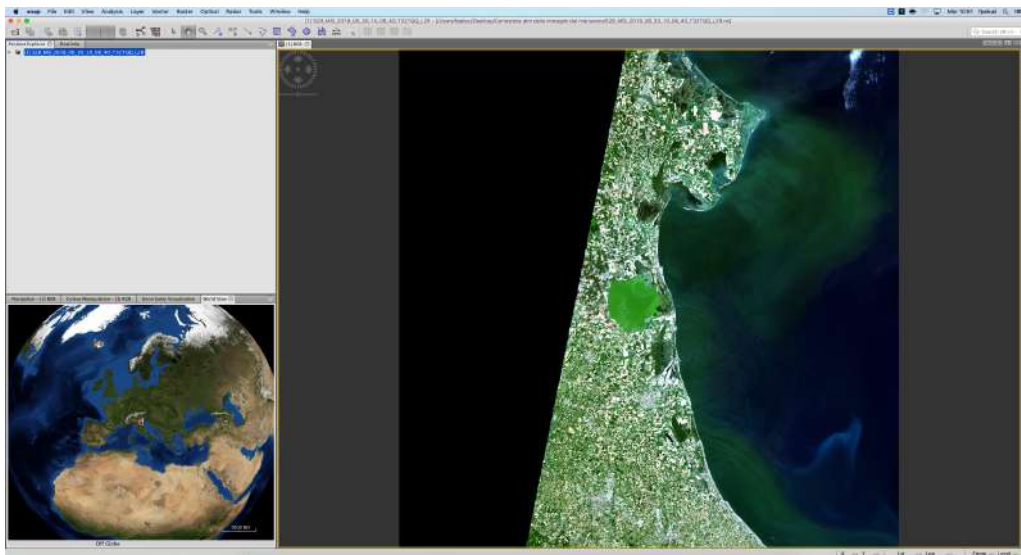


Figure 2.7: SNAP 8.0 interface

The graphical interface shows a main menu bar in the windows all the possible operations that can be performed on the images are collected:

- Analysis, allows you to choose options for statistical analysis of the image, display of scatter plots or histograms.
- Layer, contains functions with which you can create different levels on the image by superimposing pointers, grids or other
- Vector, this window gives the possibility to create vector files on the image.

- Raster, allows you to choose functions for image analysis or their treatment, it is possible to perform cut-outs, resampling, re-projection operations of the image, mosaic, texture analysis and classification.
- Optical, contains functions that allow the pre-processing of optical data and the extraction of some indices such as NDVI.
- Radar, allows you to perform all operations on the radar images, from calibration to geometric corrections up to interferometric applications

### 2.1.2 Floating debris index

At  $10\text{ m} \times 10\text{ m}$ , the highest spatial resolution of the Sentinel-2 multi-spectral instrument, individual debris elements are likely to be below detectable limits until they are patched together. To improve the detection of floating spots on the ocean surface in Sentinel-2 images, Lauren Biermann et. by 2020 they developed a floating debris index (FDI) using four of the twelve MSI bands (table 4.7)

MSI Band	Descriptor	S-2A Central Wavelength (nm)	S-2B Central Wavelength (nm)	Resolution (m)
Band 1	Coastal Aerosol	442.7	442.3	60
Band 2	Blue	492.4	492.1	10
Band 3	Green	559.8	559.0	10
<b>Band4</b>	<b>Red</b>	<b>664.6</b>	<b>665.0</b>	<b>10</b>
Band 5	Red Edge 1	704.1	703.8	20
<b>Band6</b>	<b>Red Edge2</b>	<b>740.5</b>	<b>739.1</b>	<b>20</b>
Band 7	Red Edge 3	782.8	779.7	20
<b>Band8</b>	<b>NIR</b>	<b>832.8</b>	<b>833.0</b>	<b>10</b>
Band 8a	Narrow NIR	864.7	864.0	20
Band 9	Water Vapour	945.1	943.2	60
Band 10	SWIR Cirrus	1373.5	1376.9	60
<b>Band11</b>	<b>SWIR1</b>	<b>1613.7</b>	<b>1610.4</b>	<b>20</b>
Band 12	SWIR 2	2202.4	2185.7	20

Figure 2.8: The selected bands for detecting floating debris are highlighted in bold. (Biermann et al. 2020)

This debris detection index takes advantage of the difference between NIR and the

base reflectance of NIR. This baseline is derived from linear interpolation between the RE2 and SWIR1 bands flanked by NIR:

$$\begin{aligned}
 FDI &= R_{rs,NIR} - R'_{rs,NIR} \\
 R'_{rs,NIR} &= R_{rs,RE2} + (R_{rs,SWIR1} - R_{rs,RE2}) \times \frac{(\lambda_{NIR} - \lambda_{RED})}{(\lambda_{SWIR1} - \lambda_{RED})} \times 10
 \end{aligned}$$

Figure 2.9: FDI index (Biermann et al. 2020)

The subtraction of a baseline from the NIR reflectance serves to minimise sensitivity to changes in atmosphere and observation (aerosol type and thickness, solar/viewing angle, and glint), allowing for detection of floating objects through thin cloud or haze (Hu, C. A novel ocean color index to detect floating algae in the global oceans. *Remote Sensing of Environment* 113, 2118–2129 (2009)).

Simultaneously, applied a Normalised Difference Vegetation Index (NDVI) to segregate floating vegetation from other materials.

### 2.1.3 Normalised Difference Vegetation Index

The Normalized Difference Vegetation Index (NDVI) is a simple graphic indicator that can be used to analyze the measurements obtained by remote sensing, typically but not necessarily from a special satellite, and to evaluate if the observed area contains any living vegetation (wikipedia).

The NDVI is based on the fact that vegetation, including algae, show an increase in reflectance spectra at around 700 nm( Hu, C. A novel ocean color index to detect floating algae in the global oceans. *Remote Sensing of Environment* 113, 2118–2129 (2009), Liu, D., Keesing, J. K., Xing, Q. e Shi, P. World’s largest macroalgal bloom caused by expansion of seaweed aquaculture in china. *Marine Pollution Bulletin* 58, 888–895 (2009)). The difference between reflectance values in the NIR and red serves as a measure of photosynthetic capacity and / or density of vegetation. High NDVI values indicate dense patches of floating vegetation and / or high photosynthetic activity, while water generates low to negative NDVI values (no units).

## 2.2

$$NDVI = \frac{(R_{rs,NIR} - R_{rs,RED})}{(R_{rs,NIR} + R_{rs,RED})}$$

Figure 2.10: NDVI index

### Principle of the study

In contrast to clear water, which is typically efficient at absorbing light from near infrared (NIR) to short wave infrared (SWIR), floating materials including macroalgae and macroplastics are reflected in NIR (LonnekeGodijn-Murphy et al. 2018; ChuanminHu et al. 2015...

By exploiting these spectral properties, aggregate materials floating on the ocean's surface are visible from space. Topouzel et al. 21 demonstrated this with plastic targets deployed off the coast of Mytilene in Greece. Spectra measured by drone cameras and the MSI Sentinel-2 confirmed that floating rafts made up of plastic bottles, bags and fishing nets were constantly reflecting light into the NIR. The intensity of the reflectance appeared to depend primarily on the proportion of floating plastic within the pixels. Consequently, once water makes up more than 50-70% of a given pixel, we see poor reflectance in NIR (Topouzelis et al. 2019). In the pixels filled with at least 30% of bottles or bags, or 50% of fishing net, the reflectance and absorption characteristics of the floating plastics can be observed.

Individual pieces of marine litter will likely stay below detectable limits until a front, vortex, or other undercurrent feature pulls more objects into a larger area. In the ocean, natural and man-made materials tend to be aggregated together; generating stains of mixed objects including natural sources of debris and waste dominated by macroplastics (13,25,26,27,28). Once aggregated into sufficiently large patches of various shapes and sizes, detection by Sentinel-2 is possible.

With regard to the aggregations of macroplastics in the Mediterranean, the situation is a little different. Mansu et al. (2015) was the first study to demonstrate that space-time variability in the circulation of the Mediterranean hinders the formation of stable retention areas at the basin scale. They used a simulation model with an initial homogeneous distribution of virtual particles in order to evaluate waste accumulation patterns across the entire Mediterranean basin. It identified three temporary patterns of potential accumulation, two in the northwestern sub-basin and one in the central sub-basin. It also highlighted important coastal features such as the more polluted coast,

where most of the debris ran aground (located in the southeastern Levantine sub-basin, but also between Tunisia and Syria) and, conversely, a rather low coastal impact in the western part of the Mediterranean. .

In a more recent article, *Zambianchi et al. (2017)* used the largest available set of Lagrangian historical data collected in the Mediterranean basin, together with two different initial virtual particle deployments (homogeneous and coastal distributions) to build a Markov chain model. That study found a long-term accumulation pattern in the southern and southeastern Levantine sub-basin that was similar to that encountered in the global ocean. Contrary to *Mansu et al. (2015)*, the study did not consider stranding, but only superficial circulation, which could explain the discrepancy between the two studies on the existence of long-term accumulation patterns.

Finally, *Liubartseva et al. (2018)* performed more sophisticated models to study the distribution of plastic debris in all marine compartments: on the sea surface, on the coasts and on the seabed. This study concluded that long-term accumulation patterns could not be found in the Mediterranean Sea due to general dissipative behavior on the basin. On the contrary, they identified several patterns of temporary accumulation, namely the Cilician sub-basin (northeastern Levantine), the Catalan Sea, the Po delta region and the Venice lagoon, all associated with high stranding rates.

Despite the few studies mentioned above, the modeling of plastic waste transport at sea is still in its infancy, which results in insufficient knowledge of the issue. Also, different tracking patterns, resolutions, or model configurations can sometimes lead to conflicting results.

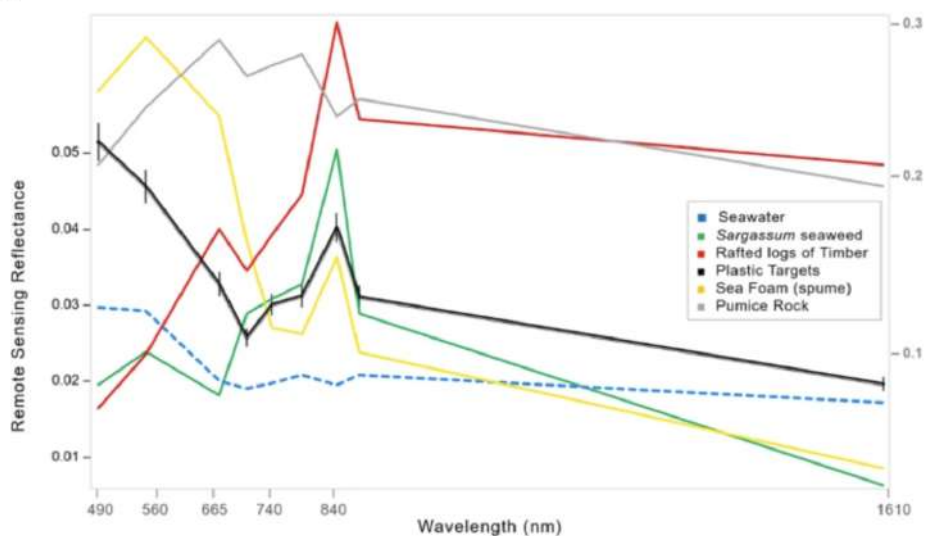


Figure 2.11: Spectral signatures derived from the mean spectra of deployed plastic targets (black line with error bars), seaweed representing floating vascular plants (green), seawater from all test sites (dashed blue line), rafted timber and wood representing non-photosynthetic plant materials (red), pumice representing non-plant debris (light grey), and spume representing sea foam, bubbles and froth (gold line). The x-axis shows the span of Sentinel-2 MSI bands from visible blue light at 490 nm, to short-wave infrared light at 1610 nm. The left-hand y-axis shows remote sensing reflectance (unitless) from Sentinel-2 for seawater, seaweed, sea foam and the plastic targets. Remote sensing reflectance (unitless) of timber and pumice was substantially higher. These were shifted lower to illustrate relative spectral shapes of all materials, and the corresponding reflectances are shown on the right hand y-axis in grey. (Biermann et al. 2020)

For remote sensing applications, spectral analysis refers to extraction of qualitative and quantitative information from the reflectance spectra of a given pixel, based on wavelength-dependent reflectance properties<sup>29</sup>. Classes of objects are therefore likely to have recognisable spectral features and characteristics, or spectral 'signatures'<sup>30</sup>. Based on absorption and reflectance patterns across 10 of the 12 Sentinel-2 MSI bands (from 490 nm to 1610 nm), we generated spectral signatures of detected seaweed, spume, timber, macroplastics and seawater. These proved key for identification of materials in mixed aggregations (Fig. 4.12) .

As illustrated in Fig. 4.12, clear water is efficient at absorbing light in the near infrared (NIR). For the Sentinel-2 MSI this corresponds to a central wavelength at approximately 833 nm. Floating plastics and plants, on the other hand, both reflect at these wavelengths. The intensity of this reflectance signal in the NIR is dependent on how much each pixel is filled by material on subpixel scales<sup>21</sup>. Plastic shows a reflectance

peak primarily in the NIR, while seaweed reflects light in the green (560 nm) and red edge (700–780 nm) bands too. Seaweed also appears to absorb SWIR light, relative to mean spectra of ocean water and plastic at 1610 nm, but variability here might be due to the atmospheric correction process. Timber shows a reflectance peak in the NIR, and also reflects relatively strongly in the red and SWIR. Pumice is noticeably bright across the optical range, reflecting in the red, red edge and SWIR, and absorbing in the NIR at approximately 833 nm. Finally, spume, which is likely to be composed of decomposing organic detritus (phytoplankton and algae, zooplankton, vascular plants), shows highest reflectance peaks in the green and red visible bands and a smaller peak in the NIR. (Biermann et al. 2020)

### **Classification of floating debris**

The detected materials were analysed within a two-variable feature space by leveraging FDI values against another band ratio, the Normalised Difference Vegetation Index (NDVI). The combination of these two band ratios provide a simplified way to analyse data while keeping most of the information content of the 6 spectral bands of the MSI sensor.

Using NDVI alone, the grouped plastics were distinguishable from seawater, seaweed, woody materials, sea foam and pumice (Fig. 4.12a). On the other hand, FDI values are primarily dependent on how much material composes a given pixel (Fig. 4.12b). When FDI and NDVI are examined together, however, materials show distinct clustering (Fig. 4.12c). (Biermann et al. 2020) The values that must be respected to have a pixel classified as plastic are shown in table 3.2. (Values indicated by the study by Biermann et al. 2020)

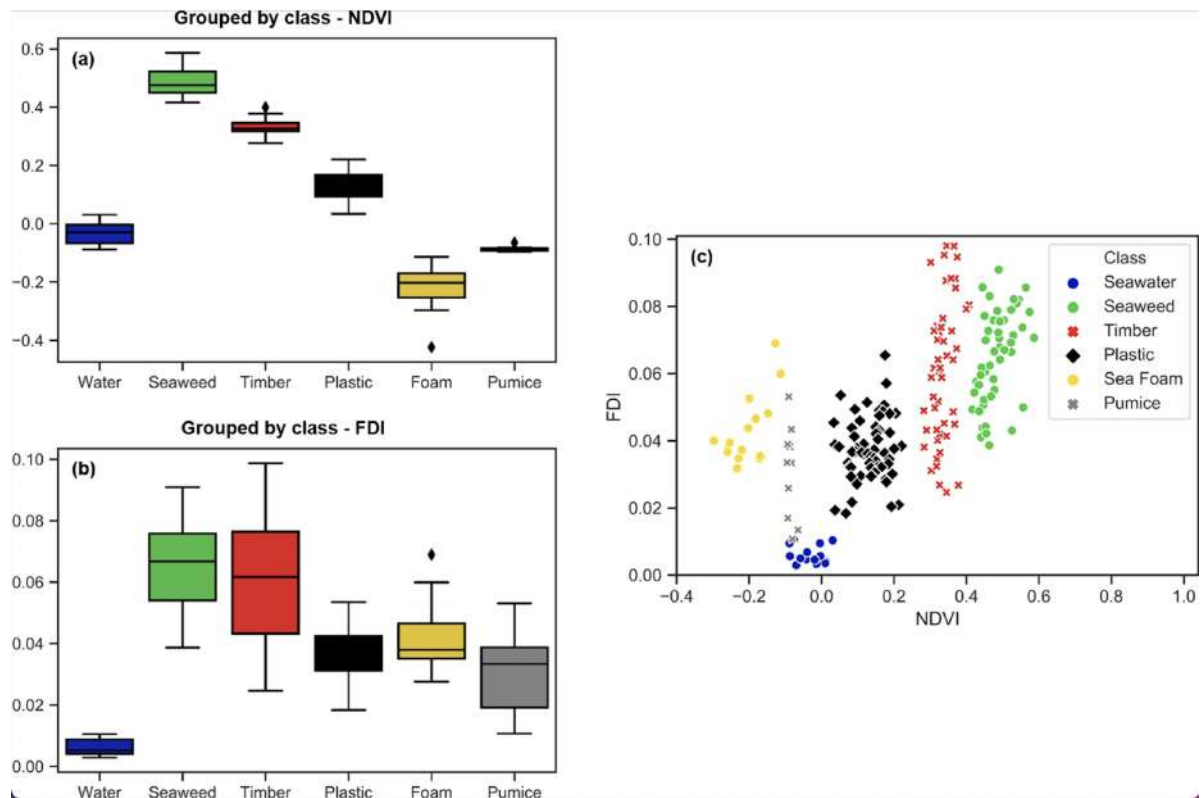


Figure 2.12: Classifying known floating materials in the marine environment. Using NDVI alone (a), we see that clear seawater (blue), wood (dark grey), spume (gold) and pumice (light grey) occupy distinct NDVI ranges that do not overlap with the combined (grouped) plastics. (Biermann et al. 2020)

## Chapter 3

# Reproduction/validation of the marine plastic debris detection methods

The experimentation described in this chapter aims to verify the effectiveness of satellite data and spectral analysis techniques currently available in the recognition of plastic waste dispersed on the surface of the water. Specifically, the interest is aimed at identifying floating macro-plastics that are transported to the Po delta exit.

The results recently obtained by Biermann et al. (2020), Topouzelis et al. (2019), & Kikaki et al. (2022), through a marine and coastal experimentation using images provided by the Sentinel 2 satellite (<https://sentinel.esa.int/web/sentinel/home>) demonstrate how the distinction between water, plastic and vegetation is possible especially considering the different reflectance peaks characteristic of the three materials in the wavelength of 840 nm, which corresponds to the near infrared (Figure 2.11). This study provides a first scientific basis that inspired the present experimentation.

The validation phase is based on ground truth data provided by the following studies: Biermann et al. 2020, Kikaki et al. 2020. and Topouzel et al. 2019. Biermann's data were used to verify the generic functioning of the methodology that will be used. Unlike the data from Kikaki and Topouzelis which were used to quantify the functioning of the technique and methodology used.

Kikaki's studio offers positioning of plastic with geographic coordinates. It must be considered that geographic coordinates are subject to errors since the measurement operations are all inevitably influenced by many factors. The study conducted by Topouzelis is a controlled experiment which consists in the positioning of three targets off the Tsamakia beach, and also in this case we know the exact position of the targets.

We studied the single pixels related to the remote sensing of artificial plastic tar-

gets floating on the sea surface with Sentinel-2 (Topouzelis 2019) and the single pixels indicated by the study of Kikaki 2022 (Marida). Trying to validate the range of values provided by Biermann (table 3.1) and the functioning of the algorithms.

<b>Range of values</b>	
<b>NDVI</b>	0.015 - 0.25
<b>FDI</b>	0.018 - 0.065

Table 3.1: Biermann range of pixel values

Figure 3.2 shows the satellite data used in this study for the validation process, with related information such as: source of reported data (i.e. basic truth and indicated by literature), as well as corresponding date and place, if available. The corresponding S2 tiles are also included for each area.

Table 3.2: The plastic debris events detected by the three studies based on satellite and in situ data. Images used for validation with related information available.

Continent/Country	S2 Tile	Source	Date	Location (WGS'84)
<b>BIERMANN</b>				
Accra, Ghana	30NZM, 30NYM		31-10-18	
Da Nang, Vietnam	Not found		30-10-19	
Gulf Island, Canada	10UDV		18-07-18	
Scotland, UK	30VWH		20-04-18	
<b>MARIDA DATASET</b>				
C.America/Guatemala	16PCC	Citizen Scientisti	18-09-20	15.836206°N, 88.022087°W
C.America/ Guatemala	16PCC	Photographer	16-06-18	15.827222°N, 88.047500°W
C.America/Guatemala	Not found	Kikaki et al.(2020)	4-09-19	14.9827°N, 89.5443°W
C.America/Honduras	16PDC	Citizen Scientistit	18-09-20	16.1490°N, 87.6282°W
C.America/Honduras	16PEC-16QED	Citizen Scientistit	23-09-20	16.042194°N, 86.432081°W
C.America/Honduras	16PEC	Kikaki et al. (2020)	29-11-15	16.0667°N, 86.3965°W
N.America/S.Domingo	Not found	Media	13-07-18	18.467723°N, 69.886808°W
Asia/Indonesia	50LLR	Social Media	4/03/18	8.715828°S, 115.446799°E
Asia/Vietnam	Not found	Social Media	23-11-19	15.994762°N, 108.27417°E
<b>TOPOUZELIS</b>				
Mytilene, Greece	35SMB		7-06-18	

### 3.0.1 The Biermann case

Biermann et al. 2020 featured case studies from four countries, selected on the basis of literature, news articles and / or posts on marine litter (representing an acute or persistent problem). The sites are: the coastal waters off Accra (Ghana), the Gulf Islands of British Columbia (Canada), Da Nang (Vietnam) and the east coast of Scotland (United Kingdom); all sites are detailed in Table 3.1. In our initial phase, we replicated Biermann's studies, starting with Ghana, which boasts a coastline that extends for about 550 km, facing the Gulf of Guinea (Figures 3.2 and 3.3). Applying the two algorithms used to Sentinel-2 data acquired on October 31, 2018, groups of bright pixels were detected along a front that traces the coast. The materials were aggregated into floating patches that ranged from about 200m to 6km offshore and appeared to be dominated by macroalgae or foam, with a number of pixels that appeared to be made up of plastic.

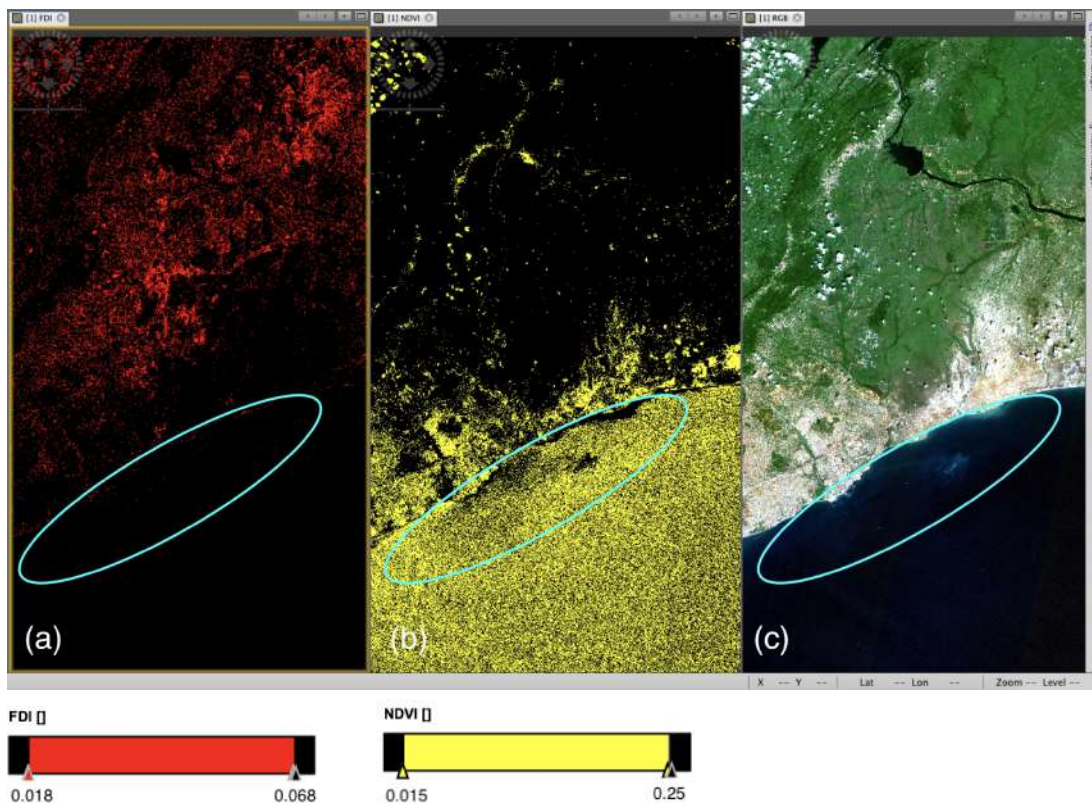


Figure 3.1: Image representing FDI-NDVI-RGB. Satellite image of the Accra, Ghana on 31 October 2018. Tile:30NZM. Time of acquisition 10:11:39, time of processing 13:56:33. Image was captured by Sentinel-2 B multispectral instrument (a) FDI (Floating Debris Index). In red all the pixels that assume the values included in the FDI range, (b)NDVI (Normalized Difference Vegetation Index). In yellow all the pixels that assume the values included in the NDVI range, (c) True color R (590-670) nm, G (500-590) nm, B (455-515)

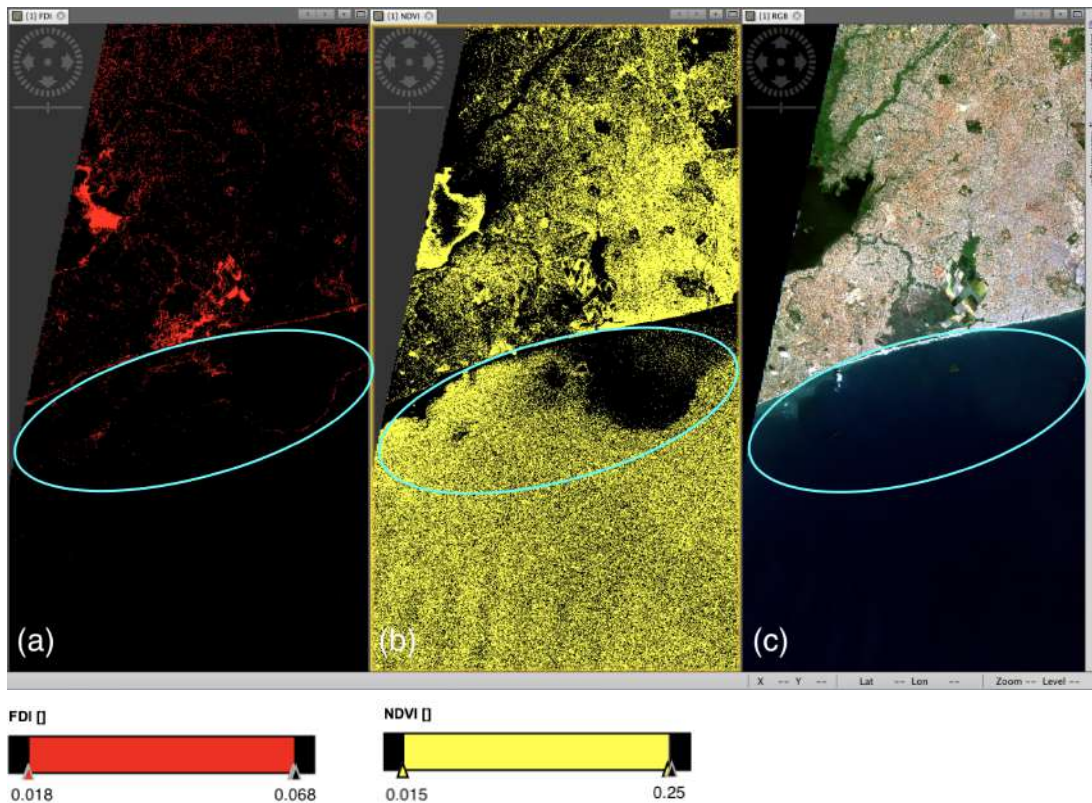


Figure 3.2: **Image representing FDI-NDVI-RGB. Satellite image of the Accra, Ghana on 31 October 2018. Tile:30NYM. Time of acquisition 10:11:39, time of processing 13:56:33. Image was captured by Sentinel-2 B multispectral instrument** (a) FDI (Floating Debris Index). In red all the pixels that assume the values included in the FDI range, (b)NDVI (Normalized Difference Vegetation Index). In yellow all the pixels that assume the values included in the NDVI range, (c) True color R (590-670) nm, G (500-590) nm, B (455-515)

Figure 3.3 depicts the Gulf Islands water zone in the Strait of Georgia in British Columbia (Canada). Applying the FDI allowed for detection of floating debris south of Gabriola Island, which is part of the Gulf Islands in the Strait of Georgia in British Columbia (Canada). In an image collected on the 18th of July 2018, bay-scale circulation appeared to entrain debris from the nearby marina, as well as woody material from timber rafting docks. A number of pixels within the detected aggregations have FDI and NDVI corresponding to the values indicated by the Biermann study for the identification of plastic.

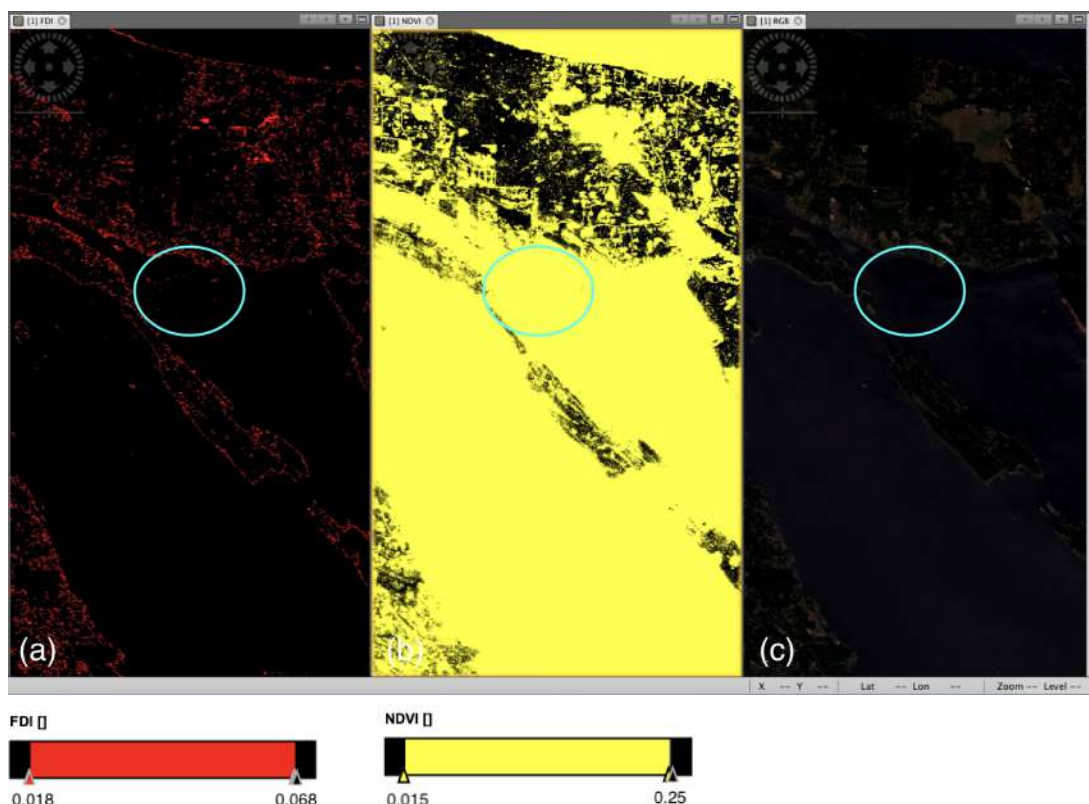


Figure 3.3: **Image representing FDI-NDVI-RGB. Satellite image of the Gulf Islands, Canada on 18 July 2018. Tile:30UDV. Time of acquisition 19:19:49, time of processing 22:37:20. Image was captured by Sentinel-2 B multispectral instrument** (a) FDI (Floating Debris Index). In red all the pixels that assume the values included in the FDI range, (b)NDVI (Normalized Difference Vegetation Index). In yellow all the pixels that assume the values included in the NDVI range, (c) True color R (590-670) nm, G (500-590) nm, B (455-515)

Figure 3.4 shows off the Scottish coast. In an image captured on April 20, 2018, the FDI application highlighted bright pixels along the edge of a strong southeastern front on the island of May. Most of the pixels appeared to be foam and algae. However, a number of pixels within the detected aggregations have FDI and NDVI corresponding to the values indicated by the Biermann study for the identification of plastic.

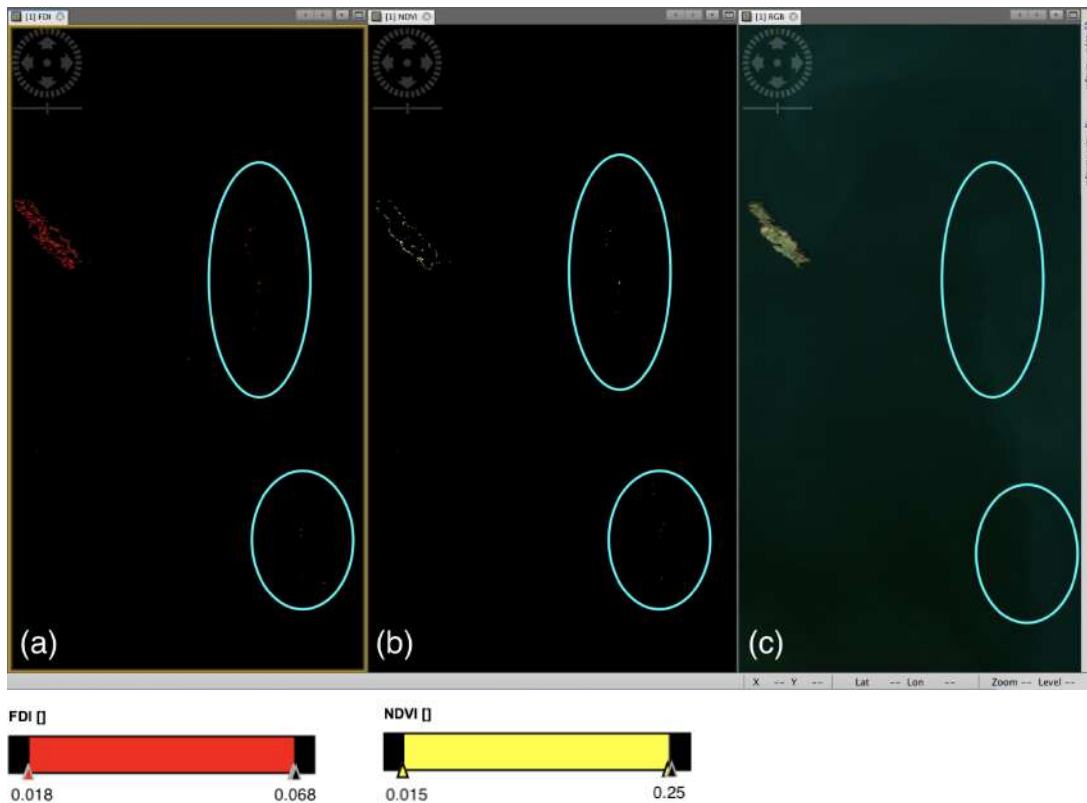


Figure 3.4: **Image representing FDI-NDVI-RGB. Satellite image of the Scotland, UK on 20 April 2018. Tile:30VWH. Time of acquisition 11:21:21, time of processing 11:44:17. Image was captured by Sentinel-2 B multispectral instrument** (a) FDI (Floating Debris Index). In red all the pixels that assume the values included in the FDI range, (b)NDVI (Normalized Difference Vegetation Index). In yellow all the pixels that assume the values included in the NDVI range, (c) True color R (590-670) nm, G (500-590) nm, B (455-515)

The 23-11-19 image of Vietnam in Asia, used by Biermann's studio after careful research, was not found.

Now, we will run tests of Biermann's study on different sites, to check the efficiency of the method. Each site we will use as a test has the presence of plastic, as we will analyze places where plastic (artificial) targets have been placed or places where the presence of plastic has been verified and measured in situ.

### 3.0.2 The Topouzelis case

Topouzel et.al.2019 led a project called "Plastic Litter Project 2018: Drone Mapping and Satellite Testing for Marine Plastic on the Aegean Sea" to explore the feasibility of detecting plastic in the aquatic environment using geoinformation acquired from unmanned aerial systems (UAS) and open access satellite missions. The experiment was conducted on 6 and 7 June 2018 near Tsamakia beach in Mytilene on the island of Lesbos, Greece.

A series of three plastic floating artificial targets (consisting of 100 m<sup>2</sup> of PET-1 1.5 liter water bottles, LDPE plastic bags and fishing ghost nets) have been set up for remote sensing in nearby waters Tsamakia beach in Mytilene on the island of Lesbos, Greece. So in this case we know the exact position of the pixel in which we have the presence of the plastic.

The image has been downloaded and processed for the validation process.

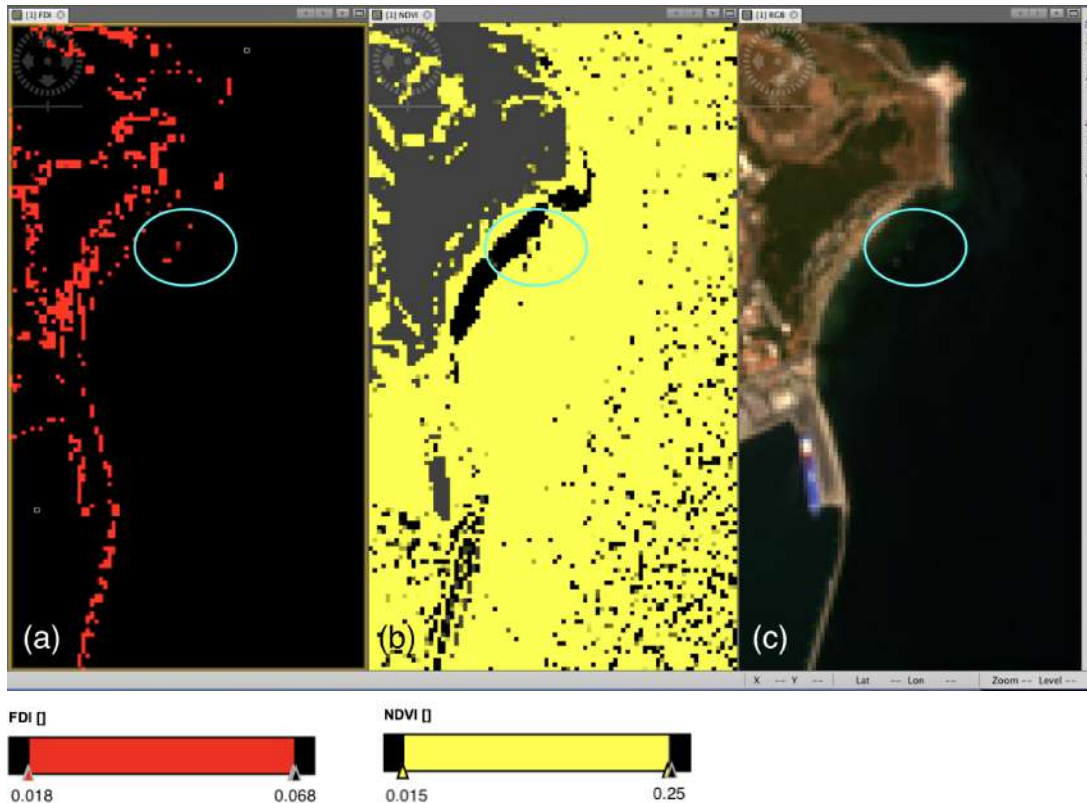


Figure 3.5: Image representing FDI-NDVI-RGB. Satellite image of Mytilene, Greece on 7 June 2018. Tile:35SMD. Time of acquisition 08:56:01, time of processing 11:05:13. Image was captured by Sentinel-2 B multispectral instrument (a) FDI (Floating Debris Index). In red all the pixels that assume the values included in the FDI range, (b)NDVI (Normalized Difference Vegetation Index). In yellow all the pixels that assume the values included in the NDVI range, (c) True color R (590-670) nm, G (500-590) nm, B (455-515)

### 3.0.3 The Marida case

Kikaki et al.2020 introduced the Marine Debris Archive (MARIDA), established on the basis of multispectral data from the Sentinel-2 satellite. Provides annotations (geo-referenced polygons / pixels) from verified events of plastic debris in different geographic regions of the world, during different seasons, years and sea state conditions. The data taken into consideration by the Marida dataset are the sites where the exact coordinates of the position of the plastic aggregates were provided.

Figure 3.6 shows the Guatemala area, in an image captured on September 18, 2020. (tile:16PCC).

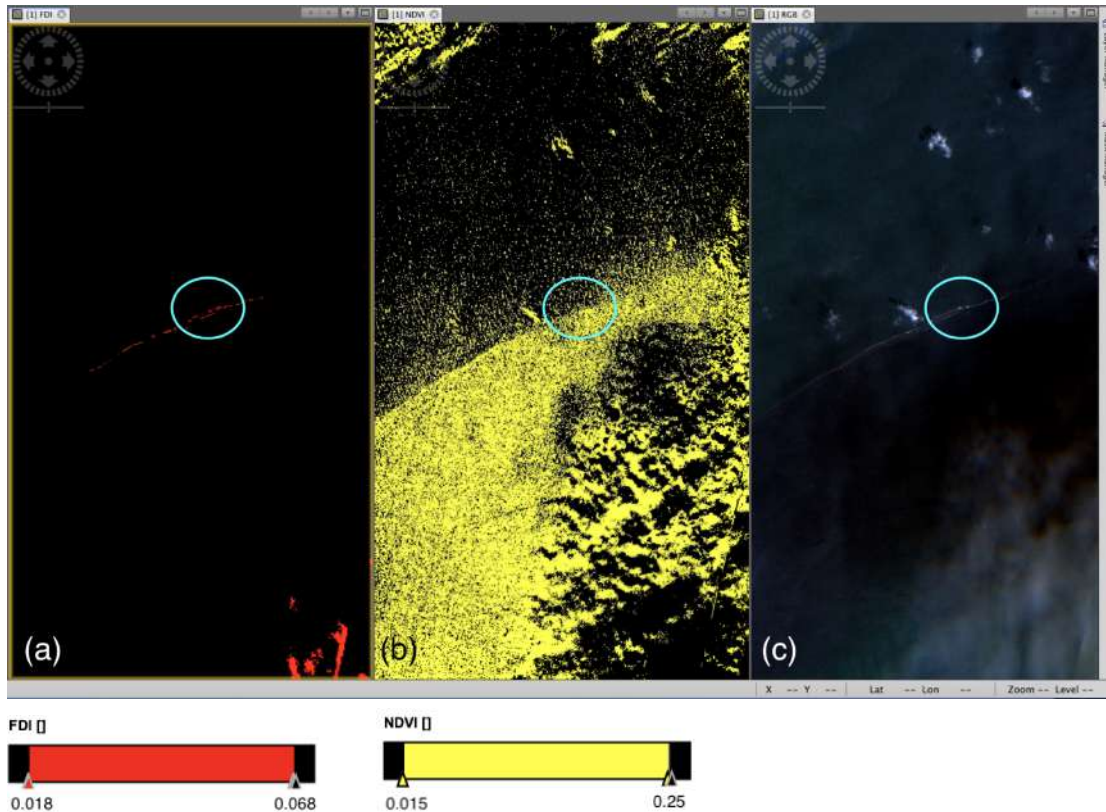


Figure 3.6: **Image representing FDI-NDVI-RGB. Satellite image of Guatemala on 18 september 2020. Tile:16PCC. Time of acquisition 16:08:39, time of processing 19:45:32. Image was captured by Sentinel-2 B multispectral instrument** (a) FDI (Floating Debris Index). In red all the pixels that assume the values included in the FDI range, (b)NDVI (Normalized Difference Vegetation Index). In yellow all the pixels that assume the values included in the NDVI range, (c) True color R (590-670) nm, G (500-590) nm, B (455-515)

The presence of a front is clearly visible in the RGB image. After applying the algorithms used and going to the geographical coordinates indicated by Marida where they reported the presence of plastic, the values confirmed this hypothesis.

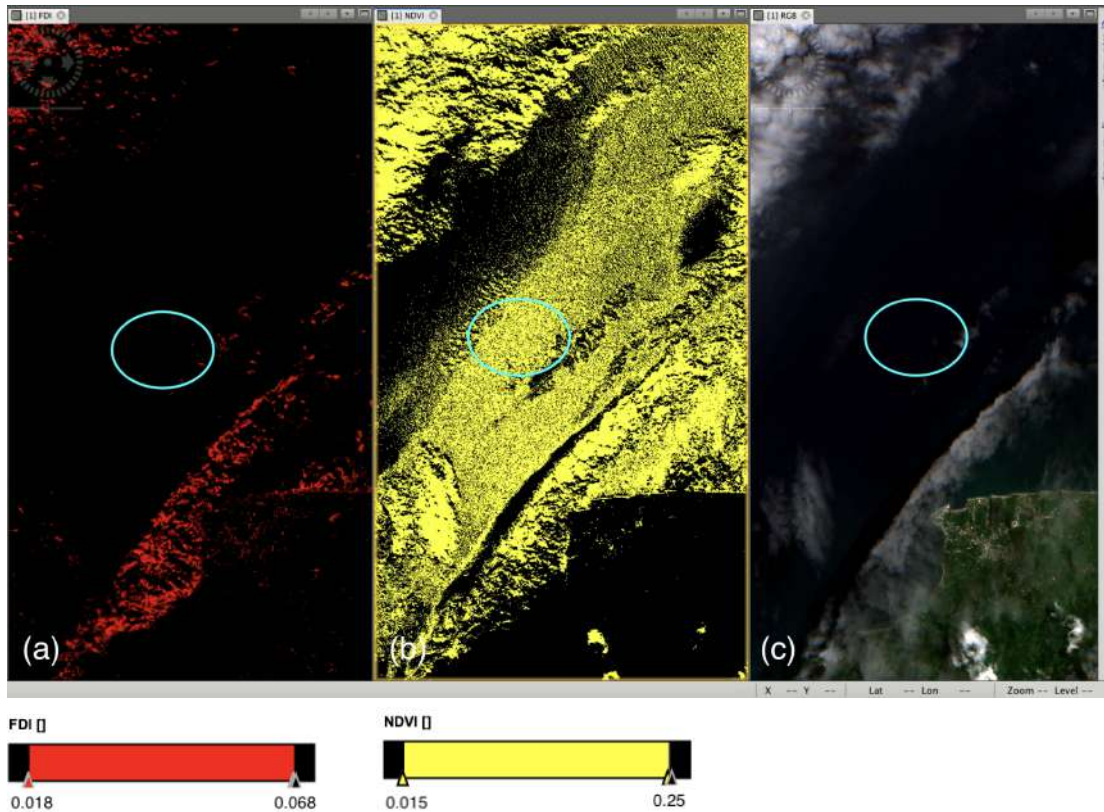


Figure 3.7: Image representing FDI-NDVI-RGB. Satellite image of C.America, Guatemala on 16 June 2018. Tile:16PCC. Time of acquisition 16:09:01, time of processing 21:19:42. Image was captured by Sentinel-2 B multispectral instrument (a) FDI (Floating Debris Index). In red all the pixels that assume the values included in the FDI range, (b)NDVI (Normalized Difference Vegetation Index). In yellow all the pixels that assume the values included in the NDVI range, (c) True color R (590-670) nm, G (500-590) nm, B (455-515)

Figure 3.7 shows the area of Central America, Guatemala captured on 16 June 2018. By applying the algorithms to the sentinel-2 satellite data, no bright pixels were detected in the coordinates indicated by Marida's study. The NDVI and FDI values do not appear to indicate the presence of plastic.

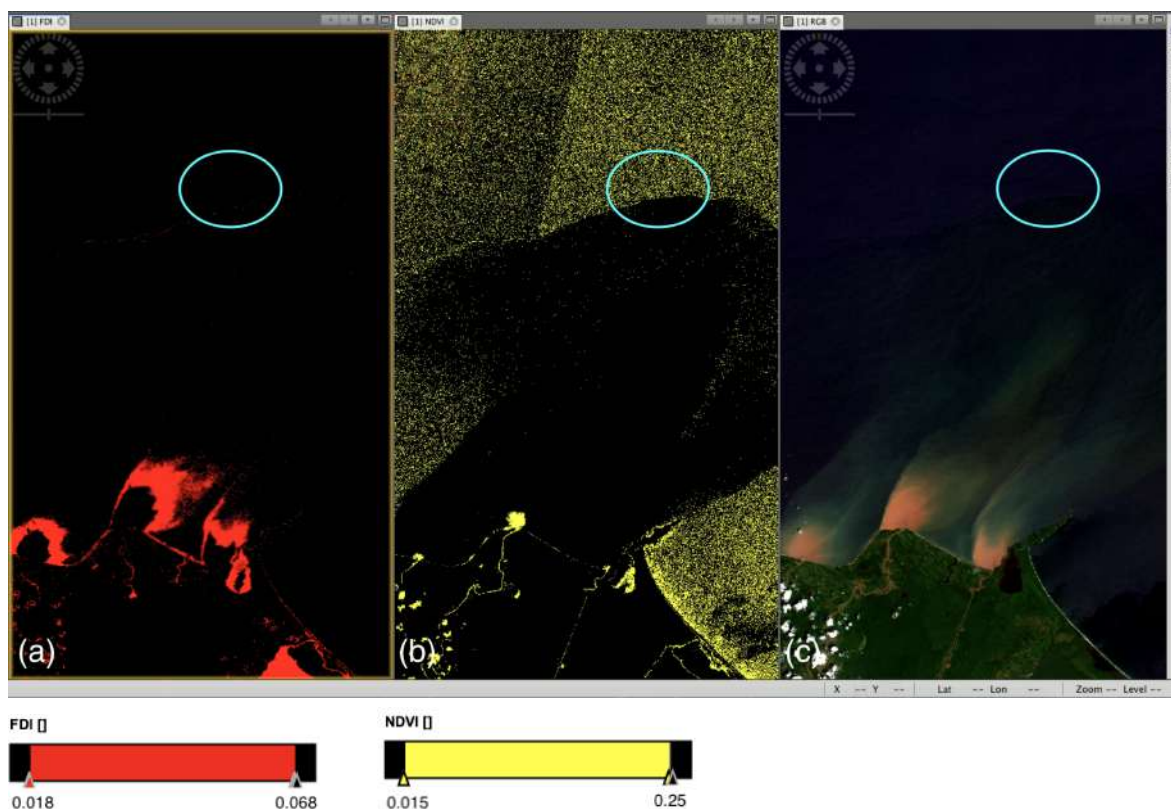


Figure 3.8: Image representing FDI-NDVI-RGB. Satellite image of C.America/Honduras on 18 September 2020. Tile:16PDC. Time of acquisition 16:08:39, time of processing 19:45:32. Image was captured by Sentinel-2 B multispectral instrument (a) FDI (Floating Debris Index). In red all the pixels that assume the values included in the FDI range, (b)NDVI (Normalized Difference Vegetation Index). In yellow all the pixels that assume the values included in the NDVI range, (c) True color R (590-670) nm, G (500-590) nm, B (455-515)

Figure 3.8 shows the C.America, Honduras captured on 18 September 2020. By applying the algorithms to sentinel-2 satellite data, no plastic was detected in the coordinates indicated by Marida's study. But just below the indicated coordinates there is a front of bright pixels some of which would indicate the presence of plastic.

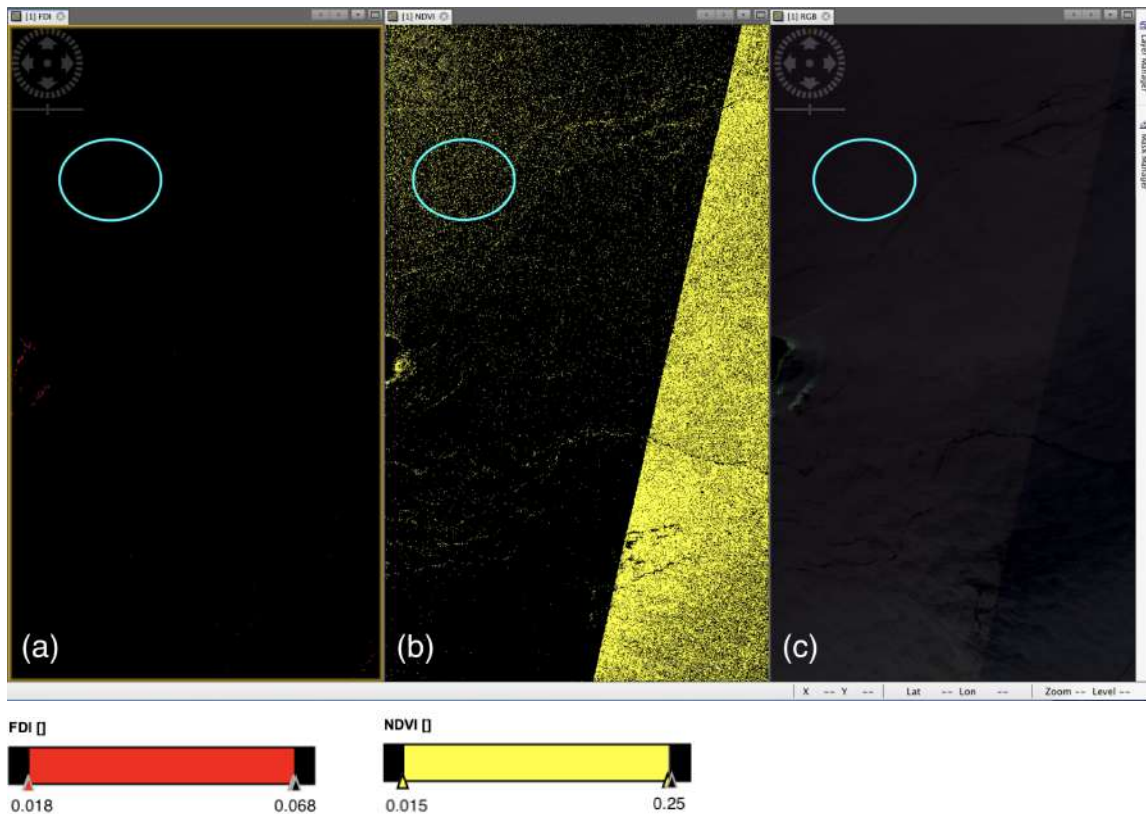


Figure 3.9: Image representing FDI-NDVI-RGB. Satellite image of C.America/Honduras on 23 September 2020. Tile:16QED. Time of acquisition 16:10:11 , time of processing 20:11:18. Image was captured by Sentinel-2 B multispectral instrument (a) FDI (Floating Debris Index). In red all the pixels that assume the values included in the FDI range, (b)NDVI (Normalized Difference Vegetation Index). In yellow all the pixels that assume the values included in the NDVI range, (c) True color R (590-670) nm, G (500-590) nm, B (455-515)

Figure 3.9 show satellite image of C.America, Honduras on 23 September 2020. By applying the algorithms to the sentinel-2 satellite data, no groups of bright pixels were detected in the coordinates indicated by Marida's study.

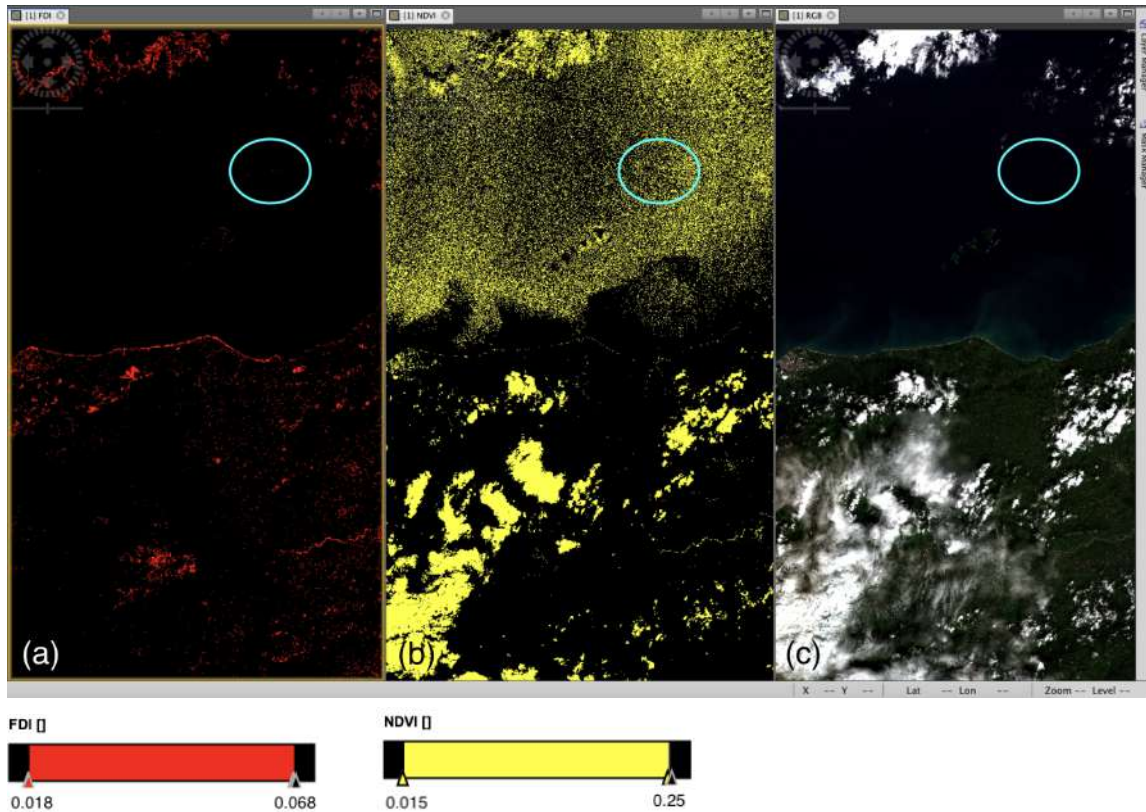


Figure 3.10: Image representing FDI-NDVI-RGB. Satellite image of C.America/Honduras on 29 November 2015. Tile:16PEC. Time of acquisition 16:16:22, time of processing 16:26:44. Image was captured by Sentinel-2 B multispectral instrument (a) FDI (Floating Debris Index). In red all the pixels that assume the values included in the FDI range, (b)NDVI (Normalized Difference Vegetation Index). In yellow all the pixels that assume the values included in the NDVI range, (c) True color R (590-670) nm, G (500-590) nm, B (455-515)

Figure 3.10 shows the satellite image of C.America,Honduras on 29 November 2015. By applying the algorithms to the sentinel-2 satellite data, no groups of bright pixels were detected in the coordinates indicated by Marida's study.

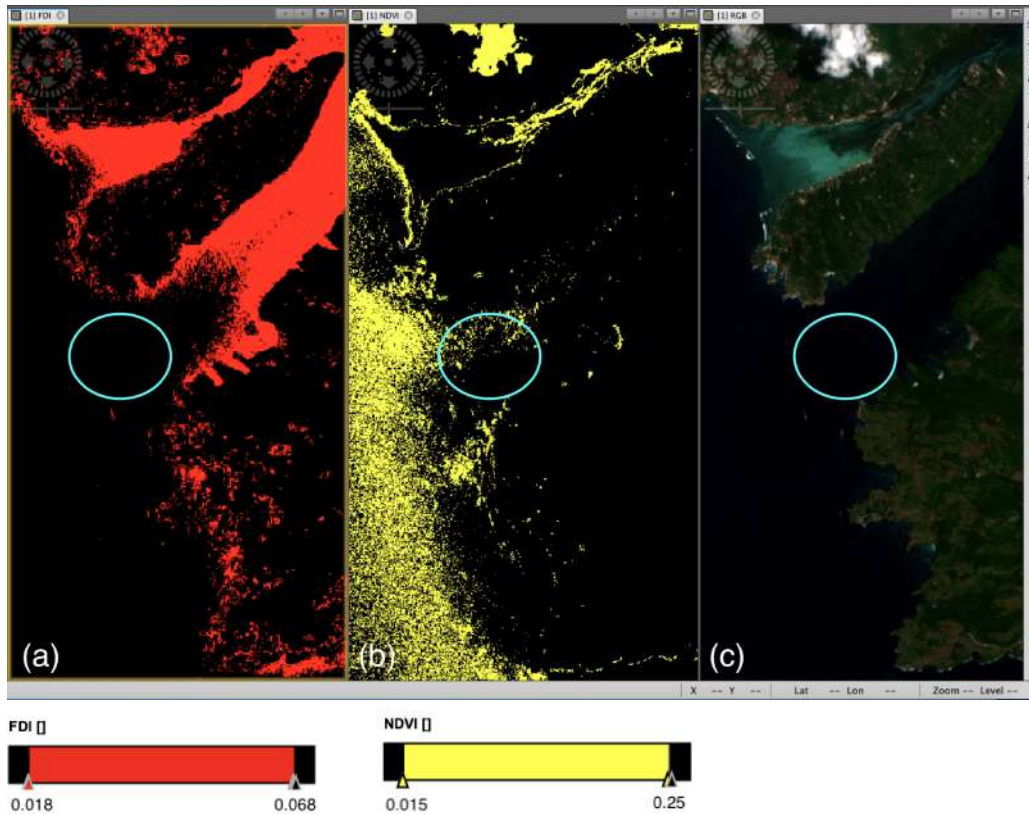


Figure 3.11: Image representing FDI-NDVI-RGB. Satellite image of Asia, Indonesia on 4 March 2018. Tile:50LLR. Time of acquisition 02:15:59, time of processing 05:50:41. Image was captured by Sentinel-2 B multispectral instrument (a) FDI (Floating Debris Index). In red all the pixels that assume the values included in the FDI range, (b) NDVI (Normalized Difference Vegetation Index). In yellow all the pixels that assume the values included in the NDVI range, (c) True color R (590-670) nm, G (500-590) nm, B (455-515)

Figure 3.10 shows the satellite image of C. America, Honduras on 4 March 2018. By applying the algorithms to the sentinel-2 satellite data, no groups of bright pixels were detected in the coordinates indicated by Marida's study.

Regarding the analysis of the targets of the Topouzelis study, for the resolution of the image, the targets are composed of 4 pixels and have a percentage of pixels of coverage of the floating plastic targets determined in the true color images captured by the Sony A5100 and the corresponding pixel spectra from Sentinel-2 images. Figure 3.14 (source Topouzelis et.al. 2019)

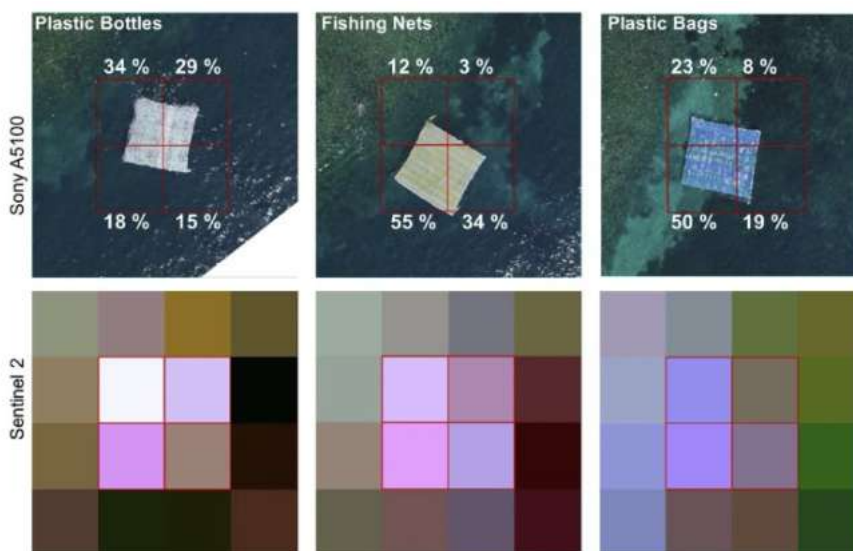


Figure 3.12: Percentage pixel coverage of the floating plastic targets

The image was viewed and analyzed via SNAP and Table 3.2 was created by taking the pixels following the legend presented in Figure 3.13.



Figure 3.13: Pixel detection legend and methodology

<b>Target 1</b>	<b>NDVI</b>	<b>FDI</b>	<b>Percentage pixel coverage</b>
1° pixel	0,13929	0,03068	34%
2° pixel	0,2216	0,02315	29%
3° pixel	-0,05135	0,00974	18%
4° pixel	0,135	0,00794	15%
<b>Target 2</b>			
1° pixel	-0,01612	0,01256	12%
2° pixel	0,0441	0,00702	3%
3° pixel	-0,21888	0,01239	55%
4° pixel	0,04441	0,00702	34%
<b>Target 3</b>			
1° pixel	0,26713	0,01043	23%
2° pixel	0,19043	0,00592	8%
3° pixel	0,28168	0,01516	50%
4° pixel	0,21198	0,00892	19%

Table 3.3: **NDVI and FDI values of the three targets.** In green the values of both algorithms that fall within the range and are consequently classified as plastic. In yellow the values that only for one of the two algorithms fall within the range. The last column indicates the % coverage of the target within the pixel.

We can state that two out of twelve pixels appear to belong to the range on both NDVI and FDI simultaneously, confirming Biermann's hypothesis, five pixels fall within the NDVI range only while all the others have values that do not belong to the range (the values are shown in table 3.3).

After analyzing the 6 images of Marida since three were not obtained due to inexistence on Copernicus, only one gave a positive response to the presence of plastic (15,836206 ° N, 88.022087 ° W). The NDVI and FDI values are shown in Table 3.4. But this result is possible that it was obtained not due to an incorrect functioning of the algorithms or an error in the ranges of NDVI and FDI considered, but probably, the coordinates provided by Kikaki's study were not precise.

<b>Marida images</b>		
<b>Date</b>	<b>NDVI</b>	<b>FDI</b>
18-09-2020	0,17528	0,03083

Table 3.4: Only verified pixel of the Marida dataset

In conclusion, by analyzing the Biermann hypothesis, we obtain a positive result (50 %) on Target 1 and negative (0 %) on Target 2 and 3. However, we must consider the fact that the three targets are made up of different types of plastic: the Target 1 is made up of bottles, the Target 2 is made up of nets and the Target 3 is made up of envelopes. Given this consideration, we can conclude that the algorithm tends to better identify the plastic of the bottles. By identifying all those pixels that have a plastic bottle coverage greater than 29% it is useless when it comes to identifying fishing nets and plastic bags.

As for Marida, one in six images had a positive outcome with regard to the Biermann hypothesis, with an overall success rate of 16.67%.

# Chapter 4

## New study cases for the Po river coastal area

The case study considered is represented by the waters coming out of the Po River.

Therefore, on the basis of the validation process carried out, a possible identification of plastic debris in the waters near the Po River delta is expected by analyzing the data acquired by Sentinel-2. The images analyzed concern the time period from 1/6/21 to 31/8/21. Not all available images were analyzed because many had excessive cloud cover. In total 17 images were considered. The satellite images used in this report, in the period of time considered, are those acquired on the dates shown in table 4.1.

2/06/21	4/06/21	14/06/21	17/06/21
22/06/21	24/06/21	29/06/21	2/07/21
7/07/21	9/07/21	22/07/21	24/07/21
29/07/21	6/08/21	18/08/21	21/08/21
26/08/21			

Table 4.1: **Aquisition Dates.** Dates in which the satellite images used in this work were acquired.

### 4.0.1 Satellite images

Among all the satellite images analyzed only in the image dating back to 26/8/21, a possible accumulation of floating material was detected, located off the Po Delta exit.

Figure 4.1 represents the large-scale location of the study area and the purple circle indicates the area where possible accumulation of floating material was detected.

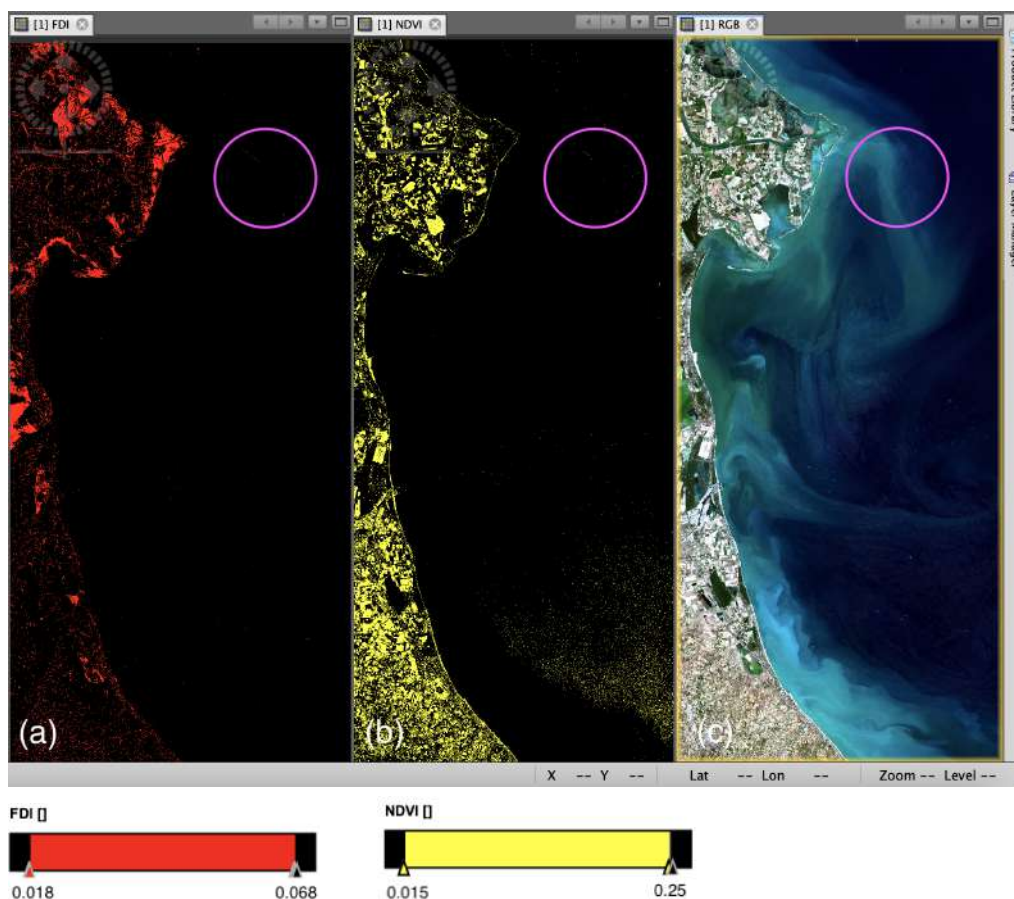


Figure 4.1: **Combined display of FDI-NDVI-RGB in large scale of the study area. The purple circle indicates the area where a possible accumulation of floating material has been detected. Satellite image of the Padana area of 26 August 2021.** Time of acquisition 10:05:49, time of processing 12:15:47. Image was captured by Sentinel-2B multispectral instrument. (a) FDI (Floating Debris Index). In red all the pixels that assume the values included in the FDI range. (b) NDVI (Normalized Difference Vegetation Index). In yellow all the pixels that assume the values included in the NDVI range. (c) True color R (590-670) nm, G (500-590) nm, B (455-515)

In picture 4.2 the possible accumulation of floating material can be observed in a close and zoomed way.

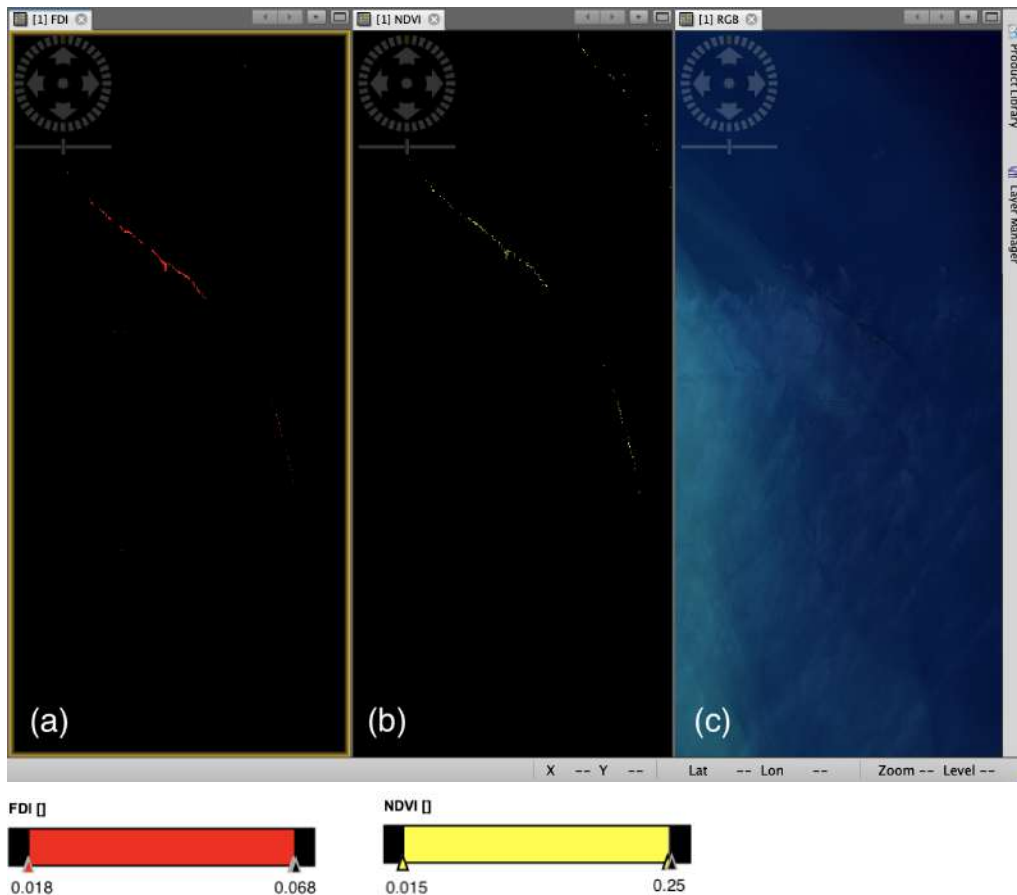


Figure 4.2: **Combined display of FDI-NDVI-RGB of the area indicated inside the circle in the previous image. Satellite image of the Padana area of 26 August 2021.** Time of acquisition 10:05:49, time of processing 12:15:47. Image was captured by Sentinel-2B multispectral instrument. (a) FDI (Floating Debris Index). In red all the pixels that assume the values included in the FDI range. (b) NDVI (Normalized Difference Vegetation Index). In yellow all the pixels that assume the values included in the NDVI range. (c) True color R (590-670) nm, G (500-590) nm, B (455-515)

At this point, to apply the classification of FDI and NDVI following the indications of Biermann, a software with the Python language has been developed, which will perform this process autonomously. The name we will give to this software is "Plastic classification", and its functionality consists in taking a .nd file, converting it into a dataset of useful information, applying the NDVI and FDI algorithms to finally perform the classification. By classification we mean the creation of a matrix  $I [i] [j]$  with  $i = 1 \dots n$  and  $j = 1 \dots m$  ( $n \times m$  is the pixel dimension of the image) which contains boolean values (0 and 1) where "1" in position  $I [i] [j]$  represents the presence of values in the Biermann range in  $NDVI [i] [j]$  and  $FDI [i] [j]$  simultaneously.

Plastic classification outputs 3 graphs: masked NDVI, masked FDI and classification. A masked matrix is a matrix without values that do not respect a certain range, in our case that of Biermann. In output, as regards NDVI and FDI, we will therefore have only the pixels that are in the Biermann range.

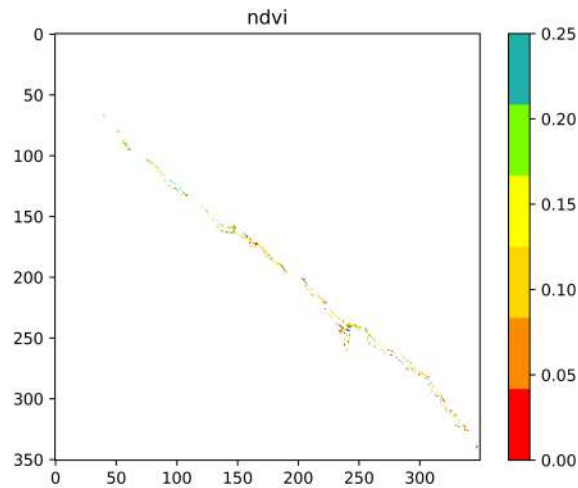


Figure 4.3: NDVI plotting containing only the pixels that fall within the specific range of values indicated in table 3.1.

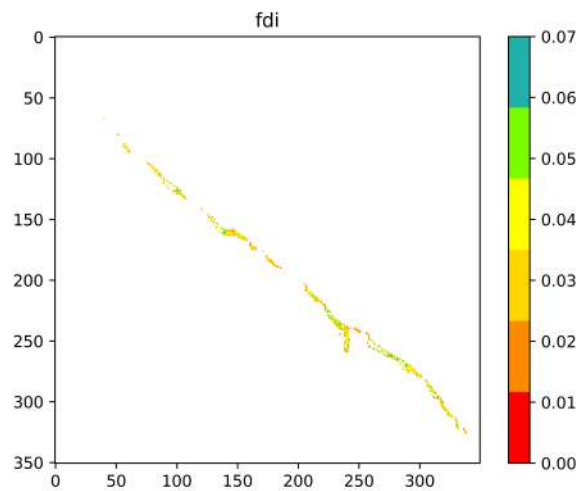


Figure 4.4: Plotting of FDI containing only the pixels that fall within the specific range of values indicated in table 3.1.

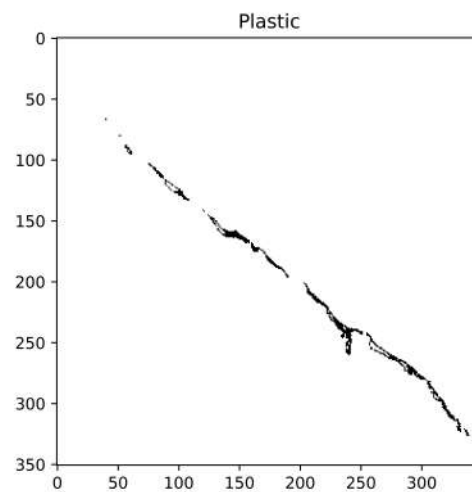


Figure 4.5: Plotting of the interpolation of the two matrices.

The pixels that appear in the last graph, we can say, are classified as plastic (plastic bottles), since the performance of the method was only good for plastic bottles. In conclusion, based on the validation results we can state that the detected pixels are classified as plastic bottle material, with at least 29% coverage of the pixel.

# Chapter 5

## Conclusions

This work focuses on verifying the detectability of plastic waste using Sentinel 2. The detectability of plastic waste using Sentinel 2 has already been tested in the marine environment (Biermann et al. 2020, Topouzelis et al. 2019, Kikaki et al. 2020).

Verification of the operation of the proposed method was carried out using ground truth point data from the studies listed above. The methodology used is based on one of the conclusions of the work carried out by Biermann (2020). Floating macroplastics can be identified within mixed aggregations in the marine environment using the combination of FDI and NDVI for a specific range of values.

To quantify the validation of this methodology, the analysis of the points of truth on the ground of the Topouzelis and Kikaki studies was carried out, which made available the geographical coordinates relating to the aggregation of verified plastic material. The validation conducted on the targets of the Topouzelis study shows us the possibility of identifying plastic bottles but not fishing nets and plastic bags. While the validation applied to Kikaki's studio allowed us to confirm only one scene indicated on the six verified scenes. The application of the methodology on the Po Valley area, in the time span studied, allowed us to identify a possible accumulation of floating plastic debris.

The experimentation confirms the possibility of using Sentinel 2 images for the visible recognition of floating debris made of plastic. On the contrary, the functioning and validation of the algorithms and methodology in question is still uncertain, requiring further experimentation. In this context, the debris identification method proposed in this study should be further expanded in order to generate more robust validation.

A more solid validation would allow not only a better calibration of the model, but also a monitoring and identification of the density of the plastic present inside the floating material, so as to be able to identify any variations in the spectral signature as a function of the variation in density of the materials present.

The method could be easily implemented and automated continuously over time in

order to create a historical series, evaluate whether to create periods with higher density of waste transported by the river that may depend on the seasonality attributable to the contribution of the river floods or if the supply of debris it may depend on other factors, further investigations could be carried out to see if marine litter has a tendency to aggregate into specific structures, for example along fronts. Specifically in the study, the proposed method for the identification of plastics should be further expanded, in order to obtain better information on the possible source of the Po River, in order to better understand the contribution of the Po on the flow of plastic into the sea.

To conclude, it would be interesting to apply the approach to a watercourse rich in wood and / or floating plastics where the validation of the model would be facilitated. Some possible applications may concern the Tiber (Italy), Rhone (France), Seine (France), Rhine (Netherlands) rivers although, according to van Calcar & van Emmerik, (2019) Indonesian and Vietnamese waterways, such as the Mekong (Vietnam) and Pahang (Malaysia) Rivers contain up to four orders of magnitude more plastic than the rivers in Italy, France and the Netherlands.

Finally, the search for floating materials through Sentinel 2 data could potentially be extended globally, even if the model would require a great deal of validation in different contexts around the globe.

# Chapter 6

## Bibliography

Biermann, L.; Clewley, D.; Martinez-Vicente, V.; Topouzelis, K. Finding plastic patches in coastal waters using optical satellite data. *Sci. Rep.* 2020, 10, 1–10.

Topouzelis, K., Papakonstantinou, A. Garaba, S. P. Detection of floating plastics from satellite and unmanned aerial systems (plastic litter project 2018). *International Journal of Applied Earth Observation and Geoinformation* 79, 175–183 (2019).

Kikaki A., Karantzalos K., Power C.A., Raitzos D.E., Remotely Sensing the Source and Transport of Marine Plastic Debris in Bay Islands of Honduras (Caribbean Sea). *Rep.* 2020, 17, 1-17.

Geyer R., Jambeck J.R., Lavender Law K, Production, use, and fate of all plastics ever made. *Rep.* 2017

Lebreton L., Andrady A., Future scenarios of global plastic waste generation and disposal. *Rep.* 2019

Annual Report UNEP, 2009

Butterworth A. , Clegg I.L.K., Marine debris: a global picture of the impact on animal welfare and of animal-focused solutions. *Rep.* 2012

Woods J.S., Rødder G., Verones F, An effect factor approach for quantifying the entanglement impact on marine species of macroplastic debris within life cycle impact assessment. *Rep.* 2019.

Derraik J.G.B., The pollution of the marine environment by plastic debris: a review (2012)

Gall S.C., Thompson R.C., The impact of debris on marine life. *Rep.* 2015

Bianchi C. Nike, Morri C., Marine Biodiversity of the Mediterranean Sea: Situation, Problems and Prospects for Future Research. *Rep.* 2000

Van Sebille E., Wilcox C, Lebreton L., Maximenko N, Denise Hardesty B., van Franeker J.A., Eriksen M., Siegel D., Galgani F., Lavender Law K., A global inventory of small floating plastic debris. *Rep.* 2015

Lebreton L., van der Zwet j., Damsteeg J-W, Slat B., Andrady A., Reisser J, River plastic emissions to the world's oceans (2017)

Schmidt C., Krauth T., Wagner S., Export of Plastic Debris by Rivers into the Sea. (2017)

Congalton R.G., A review of assessing the accuracy of classifications of remotely sensed data. (1991)

Stehman S.V., Smith J.H., Wickham J.W., Yang L., Design and Analysis for Thematic Map Accuracy Assessment. (1998)

Foody G.W., Status of land cover classification accuracy assessment. (2002)

Hu C., novel ocean color index to detect floating algae in the global oceans. Remote Sensing of Environment 113, 2118–2129 (2009)

Zanbianchini E., Trani M., Falco P. Lagrangian Transport of Marine Litter in the Mediterranean Sea. (2017)

# Chapter 7

## Acknowledgements

First of all, I would like to address my most sincere and heartfelt thanks to Professor Nadia Pinardi, supervisor of this essay, who taught me to have a critical and objective point of view and to always question myself about what I see. I thank my tutors Giovanni and Augusto, who supported me in carrying out the work.

I thank the CMCC community, who welcomed me and immediately made me feel an integral part of the team. Thank you for your availability and for your kindness.

Thanks to my family and my sister for making this possible. You have been a great support and my biggest fans. I will never forget all your sacrifices. I hope someday I can give you back some of what you gave me.

My most sincere thanks go to Omar Cocchiarella, my half, my ally, my future husband. Those who put up with me / supported me on this path, part of this milestone is thanks to him. Thank you for always being there, especially in times of desperation, for always encouraging me and for believing in me when I didn't believe it.

Thanks to all the comrades and friends I have had the honor of meeting over the years.

Thanks to ksuska, who supported me throughout the journey, supporting me and listening to me whenever I needed it.

Last but not least, I thank the third community of Silvi, a fundamental part of my life, brothers in spirit.

I really hope this article is just the beginning.